BRIGHTNESS, SPIN POLARIZATION, AND LIFETIME OF PHOTOCATHODES FOR A HIGH CURRENT ELECTRON BEAM

A Dissertation

Presented to the Faculty of the Graduate School

of Cornell University

in Partial Fulfillment of the Requirements for the Degree of

Doctor of Philosophy

by

Jai Kwan Bae

August 2022

BRIGHTNESS, SPIN POLARIZATION, AND LIFETIME OF PHOTOCATHODES FOR A HIGH CURRENT ELECTRON BEAM

Jai Kwan Bae, Ph.D.

Cornell University 2022

GaAs-based photocathodes are considered state-of-the-art for producing highly spin-polarized electron beams for accelerator and microscopy applications. Negative Electron Affinity (NEA) activated surfaces are required to extract highly spin-polarized electron beams from GaAs-based photocathodes, but they suffer extreme sensitivity to poor vacuum conditions that result in rapid degradation of quantum efficiency (QE). This thesis investigates unconventional activation recipes of GaAs using Te and Sb elements in addition to conventional Cs and O_2. Photocathode parameters, such as spectral response, spin polarization, and lifetime, are characterized for various growth recipes. To conclude the thesis, GaAs photocathodes with an optimal activation recipe (Cs-Sb-O) were characterized in a high voltage environment for a high current extraction.

Biographical Sketch

Jai Kwan Bae was born on June 18, 1991, in Seoul, South Korea. In 2016, he obtained his undergraduate degree of Bachelors of Science in Physics from the University of Rochester. During his undergraduate course of study, Jai Kwan worked on several research projects in optics and got interested in experimental physics. After finishing his undergraduate education, Jai Kwan moved to Ithaca, New York, to pursue his doctorate in Physics at Cornell University in the summer of 2016. His work mainly focused on studying and improving the operation of photocathodes under harsh conditions, such as extracting mA scale currents.

To my family: Sung Yeol Bae, Mi Ran Hwang, and Jae Hee Bae, for their unlimited support.

Acknowledgements

I have been fortunate to work on my Ph.D. surrounded by talented people always willing to help. The work presented in this thesis certainly would not have been possible without them. I cannot thank them enough for their support and contributions.

First of all, I would like to thank my advisor, Ivan Bazarov, for guiding me through my experience. He allowed me to learn, make mistakes, and develop these projects patiently. I would also like to thank my informal advisors: Jared Maxson and Luca Cultrera. Their expertise and support were invaluable during my Ph.D., and I have learned immensely from them. Alice Galdi allowed me to ask dumb questions ever since I joined the group and always has been the most approachable senior in the lab. Tobey Moore has truly magical skills to build anything we ask in time and offered great insights when it comes to designing parts for machines. Matthew Andorf has been of particular help in the last long project I participated in. It would not have been possible to conclude the project without him. I would also like to extend special thanks to Adam Bartnik, Dimitri Dimitrov, Oksana Chubenko, Joe Grames, and Marcy Stutzmann for valuable discussions.

Going through a Ph.D. would have been a lot harder without other students around me. After joining the group, William Li and I soon became the only students in the lab. Not only did we learn from each other as we explored the field, but also having another student in the group was tremendous emotional support for me. I would also like to thank other graduate students, Chad Pennington, Cameron Duncan, Chris Pierce, Mike Kaemingk, and Sam Levenson, for hanging out with me and helping me whenever I ask.

My parents Sung Yeol Bae and Mi Ran Hwang deserve the most thanks of all.

This work was supported by the Department of Energy under grants DE-SC0016203, DE-SC0019122, DE-SC0021039, DE-SC0021425, and the National Science Foundation under grants PHY-1461111, PHY-1549132.

Table of Contents

List of Tables

List of Figures

1 Introduction

1.1 Photocathode

Photocathodes are photoemissive materials that are used in electron injectors to generate electron beams for various applications. A photocathode is operated under an electric field in the range of 10's of MV/m [12] while a pulsed or continuous wave (CW) laser (200 nm ~ 800 nm) photoexcites electrons that get extracted and accelerated in the electric field.

High brightness electron source applications run the gamut in fields from high-energy nuclear physics to condensed matter physics: electron colliders [13, 14], free electron lasers (FEL) [15], beam cooling [16], and electron microscopy [17]. Electron beam brightness is the critical figure of merit for many of these applications. The brightness at the photocathode ($\mathcal{B}_{4D}$) is essentially the upper limit of the beam brightness in a photoinjector:

$$\mathcal{B}_{4D} \propto \frac{Q}{\epsilon_x \epsilon_y} = \frac{Q\, m_e c^2}{\sigma_x \sigma_y\, \mathrm{MTE}} \tag{1.1}$$

where Q is the bunch charge from the cathode, ϵ_{xy} is the normalized emittance of the beam, $\sigma_{x,y}$ is the rms laser spot size, $m_e c^2$ is the electron rest energy, and MTE

is the mean transverse energy of the photoelectrons at the photocathode [18, 19]. The laser spot size is primarily determined by the space charge beam dynamics under the electric field after photoemission. The bunch charge Q is determined by the strength of the electric field, the laser power, and the quantum efficiency of the photocathode. Quantum efficiency (QE) is a material property defined as the number of electrons emitted by the photocathode divided by the number of photons incident on the photocathode surface. QE tends to degrade over time during beam operation, and the speed of degradation is referred as an operational lifetime of the photocathode. The importance of the photocathode lifetime started gaining attention recently, especially for high average current applications.

The MTE is determined by material properties that affect the photoemission process inside the photocathode, the cathode surface, and the photoemission drive laser properties. Dowell and Schmerge demonstrated that Spicer's three-step photoemission model [20] can be utilized to derive expressions for the photoemission QE and MTE of metal photocathodes [7]. While this was originally derived under the assumption of a free electron Fermi gas and a flat density of states at zero temperature, recent studies have extended this approach to account for a realistic density of states and non-zero (but constant) electronic temperature (T_e) [9, 8]. These models predict that as the photon energy ($h\nu$) approaches the work function (ϕ), MTE converges to the thermal energy of electrons (MTE $\approx k_B T_e$). For a photon energy well above the threshold ($h\nu - \phi \gg 0$), the MTE is linear in the photon excess energy, MTE $\approx (h\nu - \phi)/3$. Both behaviors have been demonstrated experimentally [8]. These studies predict that MTE is minimized by operating with very low photon excess energy, but do not account for dynamic or intensity dependent effects, such as multiphoton excitation or

laser-induced ultrafast electron heating.

For certain applications, such as FEL and electron microscopy, response time is also an important property of a photocathode [12]. Femtosecond scale electron pulses generated from photocathode sources (this process typically involves additional compression stages downstream) play a critical role in probing time-resolved ultrafast dynamics. In particular, this property differentiates photoemission sources from thermionic and field emission sources. Thermionic sources are robust and low-cost but suffer from a high MTE and lack on/off control of the flux [21]. Field emission can provide very low MTE electron beams, but the amount of bunch charge tends to be in the order of a single electron, and the response time is slower compared to photoemission sources [22].

1.2 Photocathode materials

Photocathode materials can be classified into two groups: metals and semiconductors. Metallic photocathodes, and in particularly copper photocathodes, are popular choices for ultrafast electron sources due to their prompt response time (< 50 fs) and low vacuum requirements [23, 24]. However, compared to semiconducting emitters, they suffer from several orders of magnitude less QE ($10^{-5} \sim 10^{-6}$) due to frequent electron-electron scattering during the transport of the excited population from the bulk to the surface. Thus, metallic photocathodes can demand a very high laser intensity (10s of GW/cm^2) for femtosecond emission cases, for example, in the blowout regime[25] of high charge photoinjectors. Despite higher QE's ($1 \sim 10\%$), semiconductor photocathodes suffer from extreme vacuum sensitivity that results in a short operational lifetime.

Among popular semiconductor photocathodes, Cs_2Te is considered the most robust but requires a UV light for photoemission, while cesiated GaAs offer the highest QE at the cost of a short operational lifetime. Alkali antimonides (Cs_3Sb, K_2CsSb, NaK_2Sb) can operate in a moderate vacuum requirement with a high QE in the visible wavelengths.

Various attempts have been made in the past few decades to produce a robust photocathode with a high QE. In this paragraph, a few studies are discussed. A recent work took a data-driven approach to screen for high brightness photocathode materials. Machine learning and Density Functional Theory (DFT) were used to screen over 74,000 semiconducting materials. The study claims the family of M_2O (M=Na, K, Rb) can be potentially air-stable with desired photocathode properties, such as a low intrinsic emittance and high QE [26]. Growing an oxidized layer (MgO) on metal (Ag) has been proposed to lower the work function of the metal photocathode [27]. Later an experimental study demonstrated lowering 2 eV of work function by growing BaO_2 on Ag [28]. Perovskite materials are among the most actively studied materials in the solar cell community. However, the high work function is the main drawback for high brightness applications. Recent theoretical works predicted that some Perovskite materials could have a low work function ($1 \sim 2$ eV) [29, 30]. Various types of diamond photocathodes have photocathode properties similar to that of metal photocathodes. The cathodes tend to be very robust, but they can only operate in the UV range [31, 32]. Bi-Ag-O-Cs photocathode was reported to have a very high QE (~10%) near the photoemission threshold (480 nm) [33, 34]. Another data-driven study using DFT screened over 4,000 2D materials to find desired coating layer materials that can protect photocathodes from ion back bombardment and chemical poisoning [35, 36].

1.3 Spin polarization Photocathode

1.3.1 Applications

In 1922, Otto Stern and Walter Gerlach showed that the spatial orientation of angular momentum is quantized by splitting an atomic Ag beam depending on the spin of orbiting electrons under a nonuniform magnetic field. Since then, quantum mechanical intrinsic property spin has played an important role in understanding various phenomena in the field of physics. Recent developments on spin-polarized electrons sources have allowed broad and diverse spin-related experiments that run the gamut in fields from high-energy nuclear physics to condensed matter physics.

Future nuclear physics facility Electron Ion Collider (EIC) allows investigation of hadronic structures and exploration of new regimes of strongly interacting matter that will help to understand the fundamental quantum theory of the quark and gluon fields that constitute most visible matter in the universe [37, 38]. Since electrons do not manifest any internal structure, they are considered an optimal probe for the more complicated nucleons and nuclei. When electrons are scattered off a nucleon, a virtual photon is created that can see inside the nucleon. Since the virtual photon energy determines the resolution power, EIC is required to accelerate electrons to sufficiently high energy so that it can destroy the proton target into partons [39]. This process is called deep-inelastic scattering (DIS), and it allows the investigation of various issues that the nuclear physics community is interested in [37]. One of the issues is gluons' contribution to the total spin of a proton (1/2). Experiments at CERN demonstrated quarks and antiquarks could explain only 30% of the total spin of a pro-

ton [40]. Only an EIC with a highly spin-polarized electron beam can explore the overall spin contribution of quarks, antiquarks, and gluons combined. In a sense, EIC can be referred as the most powerful (in terms of resolution and intensity) spin-polarized electron microscope for nuclei and nucleons [39].

As opposed to EIC, if electrons have low energy ($\lesssim$ 30 eV) during the scattering, it can probe the surface structure ($\lesssim$ 0.5 nm) of single-crystals and epitaxial thin films. This technique is called Low-energy electron microscopy (LEEM), and it is one of the most commonly used routines in the condensed matter physics community. When spin-polarized electrons are used for the technique (SPLEEM), it allows a real space imaging of the magnetic domain structure on surfaces by exchange interaction [41]. Transmission electron microscopy (TEM) exploits electron scattering at the keV range (10s - 100s keV) where an electron beam is transmitted through a thin specimen ($\lesssim$100 nm) which allows high-resolution imaging (~0.05 nm) in 3D space. Coherent spin-polarized electron beam at this regime enables investigation of spin properties such as interference of spinor waves, spin-flip effects in an exchange interaction, and spin-orbit interactions. Furthermore, the Pauli exclusion principle of spin-polarized beam offers a possibility to achieve a higher contrast in TEM due to the enhanced antibunching effect [42]. Remarkably, spin-polarized electron sources in modern SPLEEM, SPTEM, and EIC are all based on GaAs technology. In the next few paragraphs, the history of state-of-art GaAs photocathode is reviewed in the light of its application in EIC particularly.

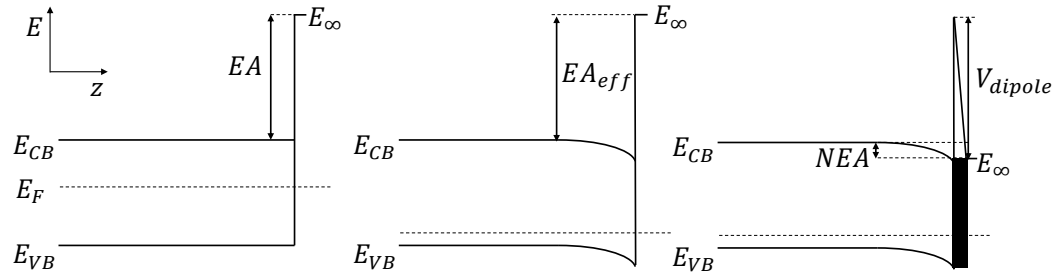

Figure 1.1: Negative electron affinity (NEA) activation process on GaAs [1]. Electron affinity (EA) is defined as the energy difference between vacuum level E_∞ and the bottom of the conduction band E_{CB}. NEA is achieved when the vacuum level is lower than the bottom of the conduction band.

1.3.2 GaAs photocathode

In 1965, GaAs was first highlighted as an attractive photocathode with the discovery of negative electron affinity (NEA) activation on the surface of *p*-type semiconductors [43]. It was demonstrated that by exposing the GaAs surface to electropositive metal, atomic cesium, a strong dipole layer can be formed that lowers the vacuum level. If the cesiated GaAs is *p*-doped, the vacuum level can be even lower than the conduction band minimum due to the downward band bending, achieving NEA (see Fig. 1.1). When the surface is NEA activated, excited electrons that have relaxed down to the bottom of the conduction band can still escape into the vacuum once they arrive at the surface, resulting in a high QE, even near the photoemission threshold.

An electron beam is considered spin-polarized when there are an uneven number of spin 'up' state electrons versus spin 'down' state electrons. The spin polarization of an ensemble of electrons can be expressed with the number of

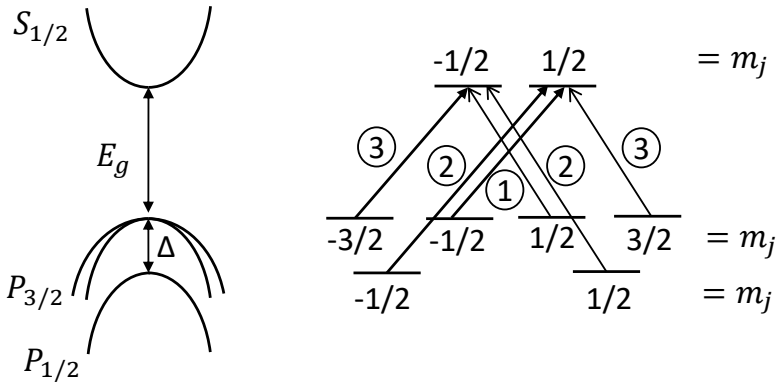

Figure 1.2: Spin dependent selection rule in GaAs [1]. The numbers next to each transition are relative ratio of transition rates. Solid line transitions require $+\hbar$ circularly polarized light while dashed line transitions require $-\hbar$ circularly polarized light.

spin-up state electrons $N_\uparrow$ and the number of spin-down state electrons $N_\downarrow$ as

$$P = \frac{N_\uparrow - N_\downarrow}{N_\uparrow + N_\downarrow}. \tag{1.2}$$

Spin-polarized photoemission from III-V semiconductor GaAs can be understood with spin-dependent selection rule in Fig. 1.2 [1]. In the energy diagram, the valence band is split into $P_{3/2}$ and $P_{1/2}$ energy levels due to the spin-orbit coupling. If photons have appropriate energy to selectively excite electrons from $P_{3/2}$ band to the conduction band with circular polarization that has $\pm\hbar$ spin angular momentum, spin asymmetry can be induced among the excited electrons. The number next to each transition is the ratio between the transition rates calculated by Fermi's golden rule [44]. Then, the spin polarization of excited electrons is

$$P = \frac{N_\uparrow - N_\downarrow}{N_\uparrow + N_\downarrow} = \frac{3-1}{3+1} = 50\%. \tag{1.3}$$

When the excited electrons are transported to the surface, the spin polarization decreases due to spin-dependent scatterings, and only ~35% of polarization is

achieved for photoelectrons at room temperature [1]. Note NEA is required to extract spin-polarized photoelectrons since the spin-dependent selection rule only allows the photoexcitation from the top of the valence band to the bottom of the conduction band.

To overcome the theoretical maximum spin polarization of 50% due to the degeneracy of light-hole and heavy-hole bands, Matsuyama *et al.* suggested using two-photon absorption so that the spin angular momentum of $\pm 2\hbar$ can be transferred to the excited electrons [45]. This would allow transition into only one of spin up or down state in Fig. 1.2. Later, it has been shown theoretically [46] and experimentally [47] that the angular momentum is only conserved under a spherically symmetric system for two-photon absorption, and measured polarization is 50% identical to the one-photon absorption case. Another attempt was to utilize the orbital angular momentum of photons in addition to the spin angular momentum [48]. However, experimentally measured spin polarization was nearly 0%. A theoretical study explains the spatial distribution of polarization pattern is concentric, and the total spin polarization averaged over the beam position would be zero [49].

The most reliable method to achieve a high spin polarization from GaAs is to exert a lattice strain aimed at breaking the valence band degeneracy between heavy-hole and light-hole bands. Both $In_{1-y}Ga_yAs$ layer grown on GaAs substrate and GaAs epitaxially grown on a $GaAs_{1-x}P_x$ buffer successfully showed a high polarization of nearly 90% at a cost of decreased photoelectron yield, or quantum efficiency (QE) [50]. The major disadvantage of exerting lattice strain is that the QE can drop by more than 2 orders of magnitude due to decreased sample thickness ($\sim 0.1\mu$m) along with isolation of the heavy hole band.

According to a recent report [39], a spin-polarized electron source should emit ~50 mA of photocurrent to achieve satisfactory performance for EIC. Quantum Efficiency (QE), or photoelectron yield, is an important property of GaAs photocathodes because increasing laser power to achieve such a high current is expensive and can damage the cathode due to heating [51]. However, as mentioned earlier, the major drawback of exerting strain on GaAs for high spin polarization is a reduced QE. Recently, a superlattice structure with distributed Bragg reflector (DBR) stack has been proposed and showed a high QE of 6.4% with a high polarization of 84% [52]. In this work, the GaAs/GaAsP superlattice structure was constructed to compensate for the decreased thickness of the strained sample. Additionally, a DBR stack (GaAsP/AlAsP) is installed under a buffer layer that serves as a Fabry-Perot cavity that reflects light back to the sample repeatedly at each layer [52].

Although excited electrons have initial spin polarization of 50% in a bulk GaAs, the measured polarization of photoelectrons is ~35% due to spin relaxation during the transport of excited electrons to the surface. In continuous wave (CW) mode, electrons in the conduction band will arrive at an equilibrium polarization P that follows

$$\frac{dP}{dt} = \frac{P_0}{\tau} - \frac{P}{\tau} - \frac{P}{\tau_s} = 0, \tag{1.4}$$

where P_0 is the initial polarization of excited electrons (50%), τ is the conduction band lifetime ($\sim 10^{-9}$s), and τ_s is the spin relaxation time. The terms represent polarization creation, polarization loss due to electron recombination, and spin relaxation, respectively. Then, the equilibrium polarization is given by [1]

$$P = P_0 \frac{1}{1 + \frac{\tau}{\tau_s}}. \tag{1.5}$$

In the case of p-type GaAs, the spin relaxation mechanism is dominated by spin

exchange interaction between electrons and holes. Then, the spin relaxation time is proportional to the temperature [1, 53]. Therefore, an operation of the electron source at a cryogenic temperature is preferred to minimize spin relaxation. In fact, it has been experimentally demonstrated that the polarization can be as high as 43% at 110 K [54].

Another approach to increase QE is via the use of the Mie resonance effect. It has been recently demonstrated that cylindrical nanopillar arrays on GaAs can induce Mie resonance, which drastically increases the scattering cross-section of light and, hence, absorption. The Mie resonances in GaAs nanopillar-array reduce light reflectivity to less than 6% from a typical value >35% [51].

The major drawback of NEA GaAs photocathode is that the activated surface suffers from extreme vacuum sensitivity because the activation layer typically forms a monolayer weakly bound to the bulk and, therefore, is chemically vulnerable. The vacuum sensitivity results in degrading of the photocathode quality, mainly quantum efficiency, which can limit the photocathode lifetime to mere hours following the cathode activation [55]. The degradation can be explained by three main mechanisms: (1) ion-back bombardment [4], (2) chemical poisoning [56], (3) and thermal desorption of the activation layer [57]. Ion-back bombardment occurs as extracted electrons ionize residual gas in the vacuum chamber, and the ionized molecules are attracted to the cathode surface and contaminate the activation layer. It has been demonstrated that extracting electrons a few mm off the electron gun center by deflecting the beam can significantly reduce ion-back bombardment by separating the contamination spot from the extraction spot [4]. For a better performance against chemical poisoning, the lifetime showed a factor of ~2 improvement when both Cs and Li are used for

electropositive metal atoms with NF_3 oxidant. If the charge extraction lifetime of a photocathode is defined as the amount of charge extracted from the cathode until QE drops by a factor of $1/e$, the current state-of-art GaAs electron gun has the charge extraction lifetime in the order of 1000 C [4]. To satisfy the current requirement mentioned earlier (50 mA) [39], one can expect the operational lifetime is only in the order of 10 hours (1000 C/50 mA) in the best case scenario. Therefore, research on improving the operational lifetime of NEA GaAs is the utmost issue for applications in future nuclear physics facilities.

Although *n*-type Cs_3Sb, Cs_2Te, and CsI were suggested [58, 59] and demonstrated [60, 61, 62] as alternative activation layers nearly five decades ago, there have been very few studies done on the performance of GaAs photocathodes activated with such layers and other alternative activation materials. Recently, Cs_2Te received attention as an alternative activation layer because Cs_2Te itself is a popular solar blind photocathode known for its robustness under harsh vacuum conditions [63]. Cs_2Te coated GaAs showed successful NEA activation [64, 65, 2] and a factor of 5 improvement in charge extraction lifetime at 532 nm without negative effects on spin polarization [55]. Furthermore, Cs-Sb-O activated bulk and superlattice GaAs were demonstrated to have an improved lifetime by a factor of 7 at 780 nm [66, 5].

In summary, the development of state-of-art spin-polarized electron source NEA GaAs photocathode is reviewed, along with a brief overview of its applications. It was reported that exerting a strain on GaAs can overcome the limit of achievable maximum spin polarization from bulk GaAs by splitting the heavy-hole and light-hole bands at the cost of significantly decreased QE. Superlattice structures with distributed Bragg reflector and nanopillar array were proposed

to compensate for the decreased QE. The major disadvantage of GaAs photocathode is the lifetime issue. Recent works have shown alternative activation methods can significantly reduce the vacuum sensitivity.

1.3.3 Measuring Spin polarization: Mott polarimeter

An electron beam is spin polarized when there are unequal number of spin 'up' state electrons and 'down' state electrons with respect to a spatial direction. Based on the spin angular momentum commutation relations, one can express the spin operator **S** with Pauli matrices $\boldsymbol{\sigma}$ as follows [67]

$$\mathbf{S} = \frac{\hbar}{2}\boldsymbol{\sigma}, \tag{1.6}$$

where

$$\sigma_z = \begin{pmatrix} 1 & 0 \\ 0 & -1 \end{pmatrix}, \sigma_x = \begin{pmatrix} 0 & 1 \\ 1 & 0 \end{pmatrix}, \sigma_y = \begin{pmatrix} 0 & -i \\ i & 0 \end{pmatrix}. \tag{1.7}$$

When an electron is in a spin state $\chi = \begin{pmatrix} a \\ b \end{pmatrix}$, the polarization in z direction can be represented by

$$P = \frac{\langle\chi|\sigma_z|\chi\rangle}{\langle\chi|\chi\rangle} = \frac{|a|^2 - |b|^2}{|a|^2 + |b|^2}. \tag{1.8}$$

Over multiple spin measurements, P can be also expressed as

$$P = \frac{N_\uparrow - N_\downarrow}{N_\uparrow + N_\downarrow}, \tag{1.9}$$

where $N_\uparrow$ and $N_\downarrow$ are the number of observed spin up electrons and spin down electrons during the measurements, respectively. Similarly, spin polarization of an ensemble of electrons is also expressed by Eq. 1.9 [67]. For example, if there is an ensemble of 10 electrons where 8 of them are in spin up state and the others

are in spin down state, 4 out of 10 electrons can be considered as unpolarized portion of the ensemble, and the rest 60% is completely polarized.

The Stern-Gerlach experiment is a historical landmark experiment that demonstrated the spatial orientation of angular momentum is quantized by splitting an atomic Ag beam depending on the spin of orbiting electrons. Although it may be intuitive to consider the Stern-Gerlach experiment set up as a method to measure the spin polarization of an electron beam, it turned out electrically charged particles experience additional Lorentz force during the splitting in a magnetic field, unlike electrically neutral Ag atoms. As a result, the beam spreading due to the Lorentz force overcomes the splitting effect from the spin orientation [68]. Such difficulties limit spin polarization to be measured indirectly based on spin-dependent interactions. The spin polarimeter based on Mott scattering is reviewed in the next few paragraphs.

Currently, the most commonly used spin polarimeters at low energies are based on Mott scattering, which is also referred as spin-orbit interaction. The coupling between electron spin and orbital angular momentum can be derived from the Dirac equation as [67]

$$H_{SO} = -\boldsymbol{\mu} \cdot \mathbf{B} \propto \mathbf{s} \cdot \mathbf{L}, \tag{1.10}$$

where $\boldsymbol{\mu}$ is the electron's spin magnetic moment, $\mathbf{B}$ is effective magnetic field, $\mathbf{L}$ is the orbital angular momentum, and $\mathbf{s}$ is the spin angular momentum. If we assume the wave function of a Mott scattered electron to be the asymptotic form of a plane wave:

$$\psi \xrightarrow[r\to\infty]{} ae^{ikz} + a'(\theta,\phi)\frac{e^{ikr}}{r}, \tag{1.11}$$

the differential cross section can be derived in terms of spin polarization [67]:

$$\sigma(\theta,\phi) = \sigma_0(\theta)[1 + S(\theta)\mathbf{P} \cdot \hat{\mathbf{n}}], \tag{1.12}$$

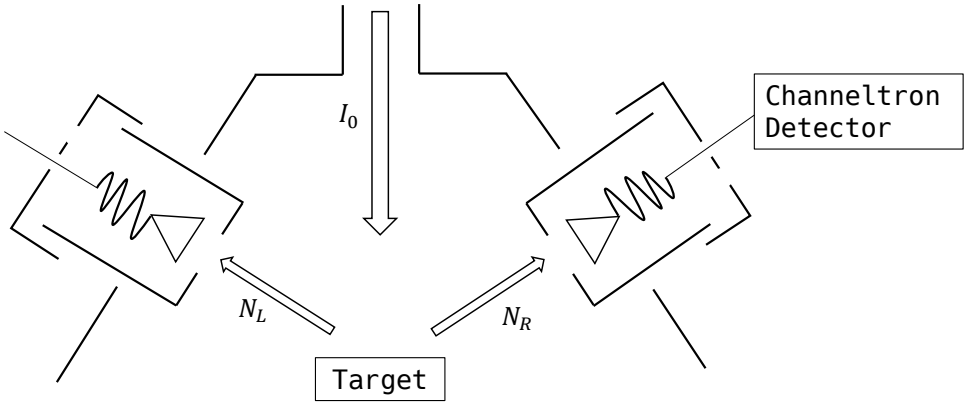

Figure 1.3: Schematic of a Mott polarimeter.

where θ and ϕ are scattering angles, and $\hat{\mathbf{n}}$ is the normal unit vector to the plane defined by initial and final momentum. σ_0 is the cross-section without spin-orbit coupling, and coefficient $S(\theta)$ is called the Sherman function. The spin dependence of cross-section allows spin polarization measurements by comparing signal intensities at two different detector positions.

Based on Eq. 1.12, a Mott polarimeter can be designed as in Fig. 1.3. During the measurements, transversely spin-polarized electron beam enters the polarimeter from electron lens assembly and gets scattered at high spin-orbit coupling target with high energy (typically ~20 keV). Heavy nuclei atoms such as gold or tungsten are common choices for the target material because the first term of perturbation expansion of Eq. 1.10 is proportional to Z^4 where Z is the atomic number [68]. Then, the scattered electrons are detected by channeltrons which work as an electron multiplier to amplify signal intensity.

When the two electron detectors are placed symmetrically, the asymmetry of

the signal intensities (N_L, N_R) due to the spin-orbit coupling can be calculated as

$$\begin{aligned} A_{SO} &= \frac{N_L - N_R}{N_L + N_R} \\ &= \frac{[1 + S(\theta)\mathbf{P}\cdot\hat{\mathbf{n}}] - [1 - S(\theta)\mathbf{P}\cdot\hat{\mathbf{n}}]}{[1 + S(\theta)\mathbf{P}\cdot\hat{\mathbf{n}}] + [1 - S(\theta)\mathbf{P}\cdot\hat{\mathbf{n}}]} \\ &= S(\theta)\mathbf{P}\cdot\hat{\mathbf{n}}. \end{aligned} \tag{1.13}$$

This equation implies that spin polarization is directly proportional to the asymmetry by the Sherman function coefficient. Although the Sherman function can be calculated theoretically based on the Mott scattering off a single atom, it is often calibrated experimentally due to multiple and inelastic scatterings using electron sources with known spin polarization such as GaAs.

Assuming the number of detected electrons N_i follows the Poisson statistics $(\Delta N_i \rightarrow \sqrt{N_i})$, the statistical uncertainty of a spin polarimeter can be calculated as [68]

$$\begin{aligned} \Delta P = \frac{1}{S(\theta)}\Delta A_{SO} &\approx \sqrt{\frac{1}{(N_L + N_R)S(\theta)^2}} \\ &= \sqrt{\frac{1}{N_0(\frac{N_L+N_R}{N_0}S(\theta)^2)}} = \sqrt{\frac{1}{N_0(\frac{I}{I_0}S(\theta)^2)}}, \end{aligned} \tag{1.14}$$

where N_0 and I_0 are the number of electrons and current entering the polarimeter, and I is the total current detected. Then, a unitless figure of merit can be defined as

$$\eta = \frac{I}{I_0}S(\theta)^2. \tag{1.15}$$

When $S(\theta)$ is substituted with a calibrated effective Sherman function S_{eff}, a state-of-art Mott polarimeter typically achieves η around 10^{-4} [69].

Designing a Mott polarimeter involves maximizing two parameters I/I_0 and $S(\theta)^2$, which depends on the energy of electrons at the moment of scattering and the scattering angle. Unfortunately, the two parameters are usually in a nega-

tive correlation [69]. As the target bias, which determines the energy of scattering electrons, increases, the effective Sherman function also increases while the detected current decreases. For the scattering angle, typically $\sim 120^\circ$ is used to maximize the effective Sherman function that prevents domination of systematic uncertainty from the Sherman function itself. Retarding potential Mott polarimeter has been recently developed: a retarding potential is applied near the detectors to screen inelastically scattered electrons that lower the effective Sherman function. Although this type of Mott polarimeter has become the most popular option due to the compact design, the figure of merit could not be improved significantly ($\eta \sim 10^{-4}$) [68]. Despite such a low figure of merit, a Mott polarimeter is the most popular option because target materials are robust and do not require maintenance.

1.4 Thesis outline

The first and last chapters of this thesis provide an introduction and summary, respectively. In chapter 2 to 4, we outline our srudies of semiconductor activation of GaAs photocathodes to improve lifetime performance for high current applications [55, 66, 70]. Chapter 5 presents a theoretical work on photoemission dynamics of Cu photocathodes under high fluence femtosecond scale laser pulses [19].

In chapter 2, we report a successful NEA activation of GaAs with Cs_2Te and confirmed it by measuring spectral response near the bandgap energy of GaAs. Auger electron spectroscopy was used to characterize the NEA surface elements. The lifetime performance of Cs_2Te activated GaAs was compared to

that of the standard Cs-O activated GaAs. Lastly, the spin polarization of each photocathode was measured with a commissioned Mott polarimeter. A similar set of measurements were performed in chapter 3 to characterize Cs-Sb-O activated GaAs photocathodes. We optimized the growth recipe using Cs, Sb, O_2 by comparing photocathode parameters of various cathodes. In chapter 4, the performance of Cs-Sb-O activated GaAs photocathode was further characterized in a high voltage DC gun for a high current extraction –the ultimate test to characterize the performance of any photocathode candidate for high average current beam applications.

Chapter 5 showcases a theoretical work where we studied the nonequilibrium thermodynamics of Cu cathode irradiated by high laser fluence. We calculated the time-dependent electron occupation function by the Boltzmann equation and estimated photocathode parameters based on Spicer's three-step model [20]. While this chapter is not related to spin-polarized beam production, the general question tackled is potentially significant for any low-emittance photocathode irradiated with a very high intensity laser pulse, including III-V semiconductor photocathodes such as GaAs.

2

Rugged spin-polarized electron sources based on negative electron affinity GaAs photocathode with robust Cs_2Te coating

This chapter was originally published as Ref. [55].

2.1 Abstract

Photocathodes capable of providing high intensity and highly spin-polarized electron beams with long operational lifetimes are of great interest for the next generation nuclear physics facilities like Electron Ion Colliders. We report on GaAs photocathodes activated by Cs_2Te, a material well known for its robustness. GaAs activated by Cs_2Te form Negative Electron Affinity, and the lifetime for the extracted charge is improved by a factor of 5 compared to that of GaAs activated by Cs and O_2. The spin polarization of photoelectrons was measured using a Mott polarimeter and found to be independent of the activation method, thereby shifting the paradigm on spin-polarized electron sources em-

ploying photocathodes with robust coatings.

2.2 Introduction

As of today, the operational lifetime of GaAs-based photocathodes remains a primary limit to the production of highly spin-polarized electron beams with high average currents. Such beams are essential to reach design luminosity for future facilities, such as the Electron Ion Collider [71], aimed at studying a wide range of phenomena from strong and electro-weak interactions to physics beyond the Standard Model [40, 72, 47].

Almost all electron sources for highly spin-polarized electron beams in accelerator physics rely on photocathode materials based on GaAs technology. By exposing the GaAs surface to a small quantity of cesium and an oxidant (oxygen or NF_3 gases are commonly used) [73], a strong dipole moment is formed at the surface that decreases the potential barrier of the electron emission into the vacuum. If the GaAs is also p-doped, due to downward pinning of the bands near the surface, the vacuum level can be lowered below the GaAs conduction band minimum (CBM) achieving the so called Negative Electron Affinity (NEA). When the NEA condition is reached, electrons that have relaxed to the bottom of the conduction band can still escape into the vacuum when they reach the surface. Such condition of GaAs results in a high Quantum Efficiency (QE) even for electrons that are excited with photon energies slightly larger than the bandgap [54].

The generation of spin-polarized photoelectrons from GaAs takes advantage of the selection rule, which conserves the total angular momentum during tran-

sitions from the valence band to the conduction band. Due to the degeneracy of the heavy-hole and light-hole band in the $P_{3/2}$ valence band state, a bulk GaAs can provide up to 50% degree of polarization depending on the doping density [1]. Several approaches have been considered to increase the degree of electron spin polarization, the most effective being implementation of a lattice strain in GaAs aimed at breaking the energy degeneracy of the light and the heavy hole bands. Indeed, strained GaAs layers grown on GaAsP produce high polarization up to 90% by splitting the degenerate energy levels at a cost of decreased QE (0.07%) using a photon energy of 1.48 eV [50]. Very recently, GaAs/GaAsP multi-layer super-lattices with a distributed Bragg reflector structure successfully showed an enhanced QE of 6.4% with a high polarization of 84% [52].

NEA GaAs photocathodes are notorious for their exceptional vacuum sensitivity. Because activation layers are extremely vulnerable to chemical reactions and weakly bound to the bulk, they require extreme high vacuum (XHV) conditions to survive a long enough time to be of any practical use. Mainly three mechanisms are responsible for the surface degradation of GaAs activated to NEA: ion back-bombardment [4], chemical poisoning [56], and thermal desorption of the activation layer [57]. The degradation of photocathode lifetime due to ion back-bombardment is proportional to the overall charge extracted from the cathode. It can be mitigated by extracting electrons from a spot several mm off the electrostatic center of the electron gun [4]. The advantages of operating under such experimental conditions have been demonstrated in the case of GaAs as well as alkali antimonides [74, 75]. When NF_3 is used as an oxidant, it was reported that activation performed using Cs and Li simultaneously can lead to improved lifetimes [76, 77]. These studies suggest that chemically stable activation layers can enhance the operational lifetime and improve the photo-

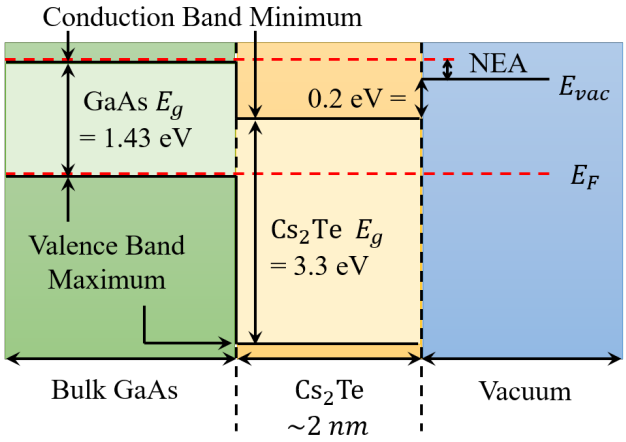

Figure 2.1: Energy band diagram of GaAs with Cs_2Te activation layer. If near IR light (~ 1.43 eV) is illuminating the sample, the photoelectrons are excited from the GaAs valence band because electrons in Cs_2Te require 3.5 eV to reach the vacuum level. NEA is formed on the surface because the vacuum level (E_{vac}) is below the GaAs conduction band minimum.

cathode's ability to better withstand both ion back-bombardment and chemical poisoning.

Cs_2Te is a well known solar-blind photocathode material. Its resistance to chemical poisoning and poor vacuum conditions is much larger than that of GaAs. Therefore, it is the most commonly used high-QE photocathode in normal conducting RF guns known for their poorer vacuum [63]. Recent studies showed that Cs_2Te could also form NEA on GaAs due to a peculiar alignment of the electronic bands of the two materials, as shown in Figure 2.1 [2, 64, 65].

In this work, we report a NEA condition produced on bulk GaAs using a Cs_2Te activation layer, the polarization measurements, and the charge lifetime obtained for these photocathodes. Our results demonstrate a more stable NEA surface as compared to the traditional activation using Cs and O_2 without negatively affecting the spin polarization of photoemitted electrons.

2.3 Growth

Several different specimens were prepared from the same highly p-doped (Zn 5×10^{18} cm^{-3}) GaAs (100) wafer. In order to remove the native oxide layer, a wet etch was performed in a 4% HCl solution for 5 minutes under the hood in the air. Then, samples were rinsed in deionized water, dried using pure nitrogen, connected to the sample holder, and loaded under vacuum in less than 1 hour. A mild sample heating at about 400 °C for 12 hours was deemed sufficient to yield a surface clean enough to perform our experiments. This was inferred from observing that after the heating, the samples could be activated to NEA using only Cs (photoemission observed with ~1.43 eV photons). The growth of Cs_2Te was performed in an ultra-high vacuum (UHV) chamber equipped with effusion cells hosting BN crucibles loaded with Cs (99.5% from Strem Chemicals) and Te (99.999% from Sigma-Aldrich). Each source is equipped with a shutter that allows to trigger on and off the flux towards the substrate surface. After the heat cleaning, the temperature of the samples was lowered to approximately 130 °C, and the light of a small diode laser operating at 532 nm was used to illuminate the negatively biased photocathode surface. The Cs_2Te growth on GaAs was performed while continuously cooling down the sample from the initial temperature of about 130 °C (see Figure 2.2 (c)). Initially, (see Figure 2.2 (a) and (b)) only a small flux of Cs was evaporated until the photocurrent is saturated for an equivalent QE of about 0.5%, which demonstrates sufficient cleanliness of the GaAs surface. At this point, the shutter for Cs was closed, and the one for Te was opened. A sharp decrease of the photocurrent was observed, followed by deposition of 0.5 nm thick Te layer as estimated from the quartz microbalance frequency shift (Figure 2.2 (b)). Another Cs deposition followed. The

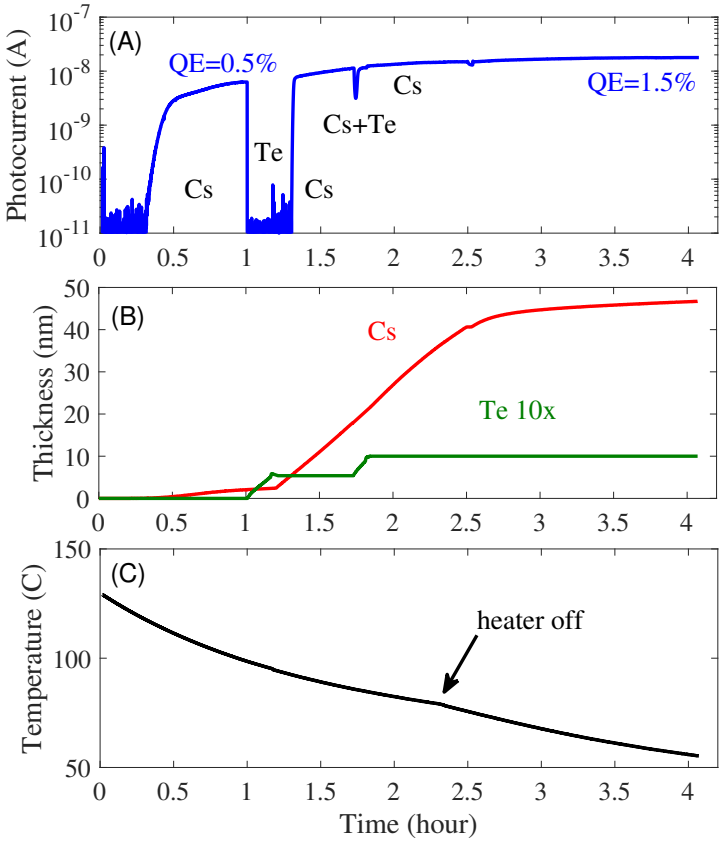

Figure 2.2: (a) Photocurrent measured over time with a 532 nm laser illuminating GaAs during alternating exposure to Cs and Te evaporation; (b) Estimated thicknesses of Cs and Te from the quartz microbalance frequency shift; (c) GaAs substrate temperature during the growth of Cs_2Te.

photocurrent increased again until an equivalent QE of about 1% was reached. Subsequent simultaneous evaporation of Cs and Te (which adds the equivalent of another 0.5 nm of Te) did not improve QE much further (Figure 2.2 (a) and (b)). Upon final cooling down, the samples were exposed to a very small flux of Cs, reaching a typical final QE of about 1.5% at 532 nm.

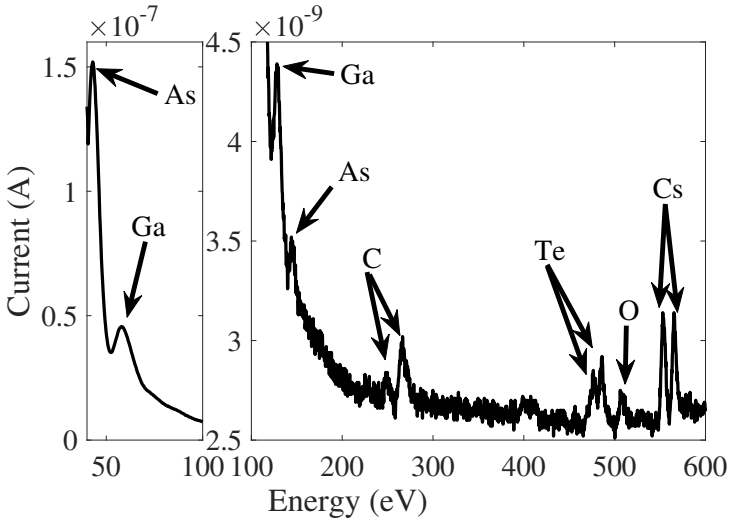

Figure 2.3: Auger electron spectra of GaAs with Cs_2Te activation layer.

2.4 Results and Discussion

One of the samples was moved under UHV into our surface analysis chamber to analyze the surface by collecting the Auger spectrum (Figure 2.3). The Auger spectra clearly show the distinctive peaks of Te and Cs confirming the presence of the two elements over the GaAs surface. Detection of Auger electrons from Ga and As also confirms that the Cs and Te layers are only a few nm thick.

The NEA condition was experimentally verified from the spectral response measurements of QE using a broadband lamp and a monochromator. Figure 2.4 shows a typical spectral response from one of our GaAs samples activated with Cs_2Te, comparing it with a similar result reported in the literature [2]. The photoemission at the photon energy of 1.43 eV (the bandgap of GaAs) supports the conclusion that the NEA condition is achieved at the surface.

Two different metrics are often used for the lifetime of a photocathode: operational lifetime, defined as the amount of time a photocathode can satisfy the

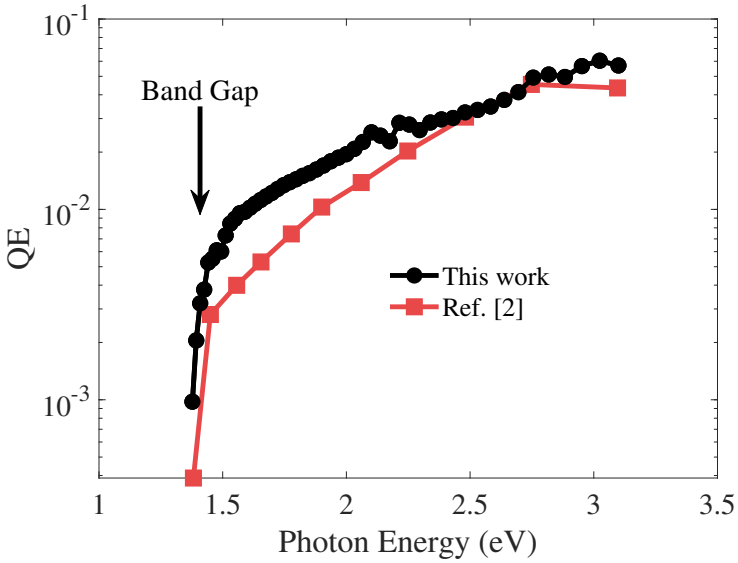

Figure 2.4: Typical spectral response of our GaAs-Cs_2Te as compared to the one from Ref.[2]

QE requirement for a particular purpose, and charge lifetime, defined as the amount of charges extracted until QE drops to $1/e$ of the initial value [4]. The latter has been suggested as a more appropriate figure of merit when comparing the performance of different photocathodes. In Figure 2.5, all lifetime measurements were performed under very similar vacuum conditions (better than 1×10^{-10} Torr) using a 532 nm laser light excitation ($\sim 50\mu$W) with identical spot size for all illuminations. After each Cs_2Te growth, the photocurrent of each sample was constantly measured until the QE went to the 1×10^{-3} level or below. Once such level was reached, the samples were exposed to a Cs flux using alkali-chromate-based dispensers to restore the initial efficiency. QEs were monitored also for the recesiated samples, and all the results are reported in Figure 2.5.

The sample coated with an activation layer grown with a 1.2-nm thin film of Te showed the largest charge lifetime value of 9.4×10^{-3} Coulomb. At the

same time, the QE at 532 nm was measured to be a factor of 2 larger than the one obtained when a 1.0-nm Te thin film was used. Compared to the lifetime of 1.9×10^{-3} Coulomb measured for a GaAs activated with Cs and O_2, the Cs_2Te layer enhanced the lifetime by a factor of 5 in our experimental conditions. While the exposure to Cs vapors was effective in restoring QEs to even higher levels than the original ones, the charge lifetimes of the recesiated samples are considerably shorter than the original ones. The recesiated samples had charge lifetimes comparable to those of the Cs and O_2 activated ones. This suggests that Cs atoms did not penetrate deeply and/or react with the Cs_2Te layer but rather deposited on the surface after the recesiation.

Despite the fact that our experiments were performed under UHV conditions, all the charge lifetimes that were measured appear orders of magnitude lower than those reported for GaAs activated to NEA that operated in one of the CEBAF electron guns with a beam energy of 100 keV [78]. A simple explanation to this experimental result is related to the vastly different experimental conditions we had in our case. Indeed, unlike the CEBAF gun where the electron beam is accelerated to 100 keV, photoelectrons in our setup are accelerated to mere ~40 eV. At such low kinetic energies, the electron impact ionization cross-section for molecular hydrogen (which is considered to be the dominant chemical species in the residual gas of the vacuum chamber) is 3 orders of magnitude greater than that at 100 keV [4, 78]. Also, due to the lack of any deflecting fields, electrons and ions trajectories are co-linear, so that the flux of back-streaming ions is likely to impact at the exact location where the laser spot is illuminating the photocathode. Finally, the positive ions are accelerated at relatively low energies, and hence they will mostly damage a very shallow region near the surface rather than penetrating deeper into the bulk, i.e. affecting the layers

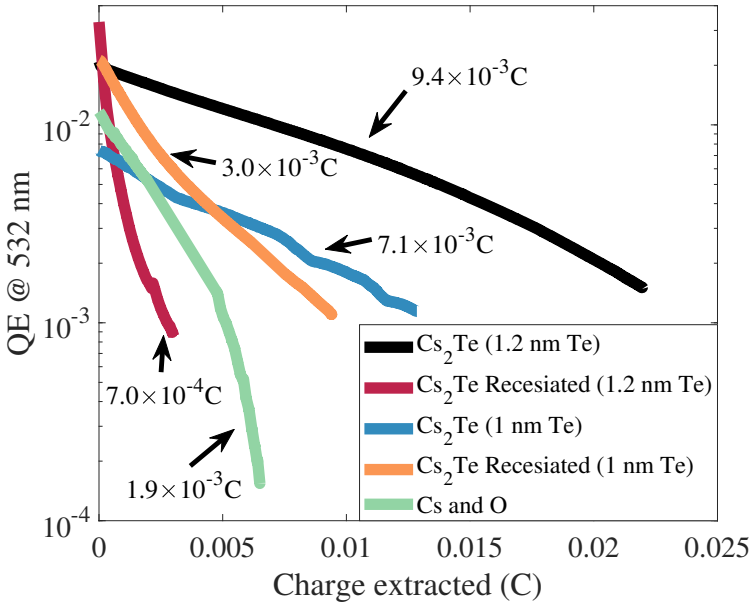

Figure 2.5: Quantum Efficiency of GaAs with various surface conditions at 532 nm wavelength as a function of extracted charges. The number next to each curve is the charge lifetime obtained from an exponential fit.

responsible for the NEA more effectively.

The photocathode laboratory UHV installation has been upgraded with a low energy reflection mode Mott polarimeter that was originally part of SLAC photocathode test-stand [79]. This Mott analyzer's Sherman function was characterized to be $S_{\text{eff}} = 0.15$ at 20 kV operating voltage with a 5% accuracy when electrons within a 1 keV energy loss window are allowed to be detected [80]. Monochromatic light was circularly polarized using a linear polarizer (Thorlabs LPVIS050) and a liquid crystal variable wave plate (Thorlabs LC1113B), and it was directed unto the sample surface at normal incidence. The helicity of circular polarization was switched by alternating retardance of the liquid crystal wave plate between $\frac{1}{4}\lambda$ and $\frac{3}{4}\lambda$.

One of GaAs samples was first activated to NEA using Cs and O_2, and then moved into the UHV chamber equipped with the Mott polarimeter. Photoelectrons were transported to the Mott detector, and from the measured asymmetries in the scattering process and the known value of the S_{eff}, the electron beam polarization was obtained for different wavelengths. See Figure 2.6. The measured values agree quite well with those recently reported for similar bulk GaAs by another group [1]. The same sample was then moved back to the Cs_2Te growth chamber. There it was first heated for 12 hours at 400 °C to remove the Cs and O_2 from its surface, and then Cs_2Te thin film was deposited on it. Once the GaAs sample was activated with Cs_2Te, it was moved back to the Mott chamber to measure the spin polarization of photoelectrons. Results are reported in Figure 2.6 as well. We found that the Cs_2Te thin film did not affect the polarization of the photoelectrons from GaAs.

Although the maximum theoretical electron spin polarization achievable for bulk GaAs is 50%, due to spin relaxation mechanisms happening before the emission into vacuum, 30-40% degree of polarization is usually attained from NEA GaAs. For GaAs, electron spin relaxation mechanisms have been extensively studied and are dominated by the lack of inversion symmetry and the exchange interaction between electrons and holes, leading to a characteristic relaxation time τ_s of ~100 ps at room temperature [81, 82, 53]. Additional depolarization mechanisms at activation layers are relatively unknown and have been considered negligible because the Cs and O_2 activation is on the order of less than a monolayer. In case of Cs_2Te activation layer, the thickness might be no longer negligible, and the activation layer can become an additional source of spin depolarization. Based on Refs. [82, 53], we estimate τ_s to be similar to that of GaAs but dominated by the lack of inversion symmetry and the spin-orbit

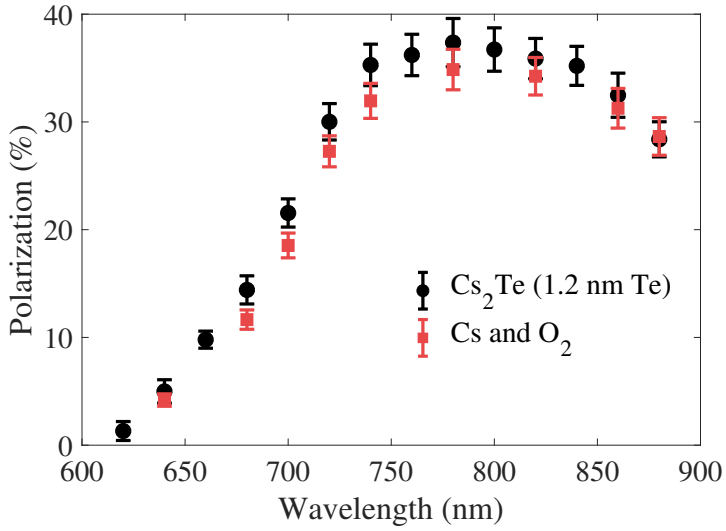

Figure 2.6: Spin polarization measured from GaAs samples activated by Cs_2Te and Cs and O_2 as a function of the laser wavelength.

coupling due to a heavier electron effective mass. The conduction band electron effective mass of $1.1m_e$ at Γ point was used based on calculations [83]. From this estimate, we expect that electrons can travel several tens of nm in Cs_2Te without experiencing significant depolarization. Our results reported in Figure 2.6 support this conclusion.

An electron mean free path of 3 nm and mean energy losses of 5 meV have been used to accurately reproduce the spectral response of Cs_2Te using Monte Carlo techniques [84]. Assuming 0.15 eV as the maximum energy of electrons excited in GaAs with 780 nm light and injected into the Cs_2Te layer (see Figure 2.1): electrons should still be able to escape even after having experienced on the order of 30 (= 0.15 eV/5 meV) scattering events. Making the assumption of small scattering angles [85], a few tens of nm of Cs_2Te should also not drastically affect the efficiency of electron emission.

2.5 Conclusion

In conclusion, we activated GaAs with Cs_2Te to study their effect on NEA formation, lifetime, and spin-polarization of the photocathode. NEA condition was confirmed by the spectral response. The lifetime showed a factor of 5 improvements while the spin polarization remained the same as the one obtained with the Cs and O_2 standard activation. Based on our presented results and simplified estimates predicting negligible losses of quantum efficiency and spin polarization, we plan to experiment with a thicker Cs_2Te to further improve the photocathode lifetime. We believe that our work triggers a paradigm shift in activating GaAs photocathodes with other materials that can both form more robust NEA activation layers and enable applications requiring high spin-polarized photoelectrons.

2.6 Acknowledgments

This work is supported by DOE Grant No. DE-SC0016203 and NSF PHY-1461111. The authors wish to acknowledge T. Maruyama, M. Stutzman, and M. Poelker for fruitful discussions and help in recommissioning the Mott polarimeter.

3

Improved lifetime of a high spin polarization superlattice photocathode

This chapter was originally published as Ref. [66].

3.1 Abstract

Negative Electron Affinity (NEA) activated surfaces are required to extract highly spin polarized electron beams from GaAs-based photocathodes, but they suffer extreme sensitivity to poor vacuum conditions that results in rapid degradation of quantum efficiency. We report on series of unconventional NEA activations on surfaces of bulk GaAs with Cs, Sb, and O_2 using different methods of oxygen exposure for optimizing photocathode performance. One order of magnitude improvement in lifetime with respect to the standard Cs-O_2 activation is achieved without significant loss of electron spin polarization and quantum efficiency by codepositing Cs, Sb, and O_2. A strained GaAs/GaAsP superlattice sample activated with the codeposition method demonstrated similar enhancement in lifetime near the photoemission threshold while maintaining 90% spin

polarization.

3.2 Introduction

Highly spin polarized electron beams with high currents are required by future nuclear physics facilities such as the Electron Ion Collider and the International Linear Collider [71, 40, 72]. Photocathode sources capable of providing spin polarized electron beams at high currents (~ 50 mA) [39] for extended period of time which are robust against less than ideal vacuum conditions are required in order to reduce the cost and complexity of operating these new facilities. Long lifetime polarized electron sources are also of interest for electron microscopy technologies that exploits spin polarization to probe magnetization in materials and nanostructures at the nanoscale level. Additionally, bright spin polarized sources driven with a short pulse laser can enable time studies of magnetization dynamics [86, 17, 87]. GaAs-based photocathodes are the present state of the art for the spin polarized electron sources because they can provide highly spin polarized electron beams with high efficiency [52]. However, their short operational lifetime poses limits particularly for applications requiring high average current [88].

GaAs was first shown to be an attractive electron photoemitter five decades ago via the discovery of negative electron affinity (NEA) activation on *p*-type samples [43]. When the GaAs surface is exposed to cesium vapor (electropositive metal atoms), a strong dipole layer is formed on the surface that lowers the electron affinity, which is defined as the energy difference between the vacuum level and conduction band minimum [1]. If the GaAs is *p*-doped, the effective

electron affinity can become negative because of the downward band bending near the surface. Thus, in NEA conditions, electrons that have relaxed to the bottom of the conduction band after photoexcitation can still escape into vacuum when they reach the vacuum interface. The combination of NEA and other characteristics of GaAs-based photocathodes, such as high electron mobility, results in a high quantum efficiency (QE) at the band gap photon energy of about 1.4 eV [44]. Additionally, it was demonstrated that the introduction of an oxidant, such as oxygen or NF_3, during cesiation can yield an even stronger dipole moment layer and achieve larger NEA and hence larger QE [89, 73].

Spin polarized electron photoemission from GaAs is achieved by exploiting the quantum mechanical selection rule that conserves the total angular momentum during photoexcitation with circularly polarized light [44]. Since electrons need to be excited only from the top of the valence band for a high spin polarization, NEA is required. Due to the degenerate light-hole and heavy-hole band states in the $P_{3/2}$ valence band, the theoretical limit of spin polarization of NEA bulk GaAs is 50%. Additionally, various spin relaxation mechanisms limit spin polarization from bulk GaAs to $\sim$ 35 % at room temperature [1]. A number of approaches have been proposed to overcome this limit [48, 47]. where exerting lattice strain on GaAs aimed at breaking the valence band degeneracy has been the most successful [50]. This method exhibits a high spin polarization of 90% but suffers from significantly decreased QE of 0.07%. In an extension of this approach, GaAs/GaAsP multi-layer superlattices structures with a distributed Bragg reflector were shown to improve the QE up to 6.4% with a spin polarization of 84% [52].

NEA surfaces of GaAs suffer from extreme vacuum sensitivity because tradi-

tional activation layer materials such as Cs-O_2 and Cs-NF_3 form about a monolayer that is weakly bound to the surface and is chemically reactive [57, 56]. Enhancement of activation layer chemical stability has been shown by using two alkali species, Cs and Li, during activation [77, 76, 90]. While the chemical reactivity is responsible for QE degradation when no photoemission is occurring (dark lifetime), the ion back-bombardment effect also limits the lifetime of the GaAs-based photocathodes during beam extraction. Deflecting the electron beam near the emission site was proposed to counteract this mechanism and showed an improvement in lifetime of both GaAs and alkali antimonide photocathodes [4, 75, 91, 74].

Although *n*-type Cs_3Sb and CsI were demonstrated to be alternative activation materials at the time of the discovery of NEA activation [58, 59, 61, 62, 60], they have generally been avoided in the photocathode community because the semiconductor activation layer is thicker, and can potentially decrease spin polarization. Recent studies reported successful NEA activation on bulk GaAs using Cs_2Te [64, 65, 2], a semiconductor known for being a robust solar blind photocathode material itself [63]. It was demonstrated that a Cs_2Te activation layer can improve the charge extraction lifetime by a factor of 5 without negatively affecting the spin polarization [55]. Yet, all experiments were done with bulk GaAs, which only has up to 40% spin polarization at room temperature. Activation of high spin polarization photocathodes (like GaAs/GaAsP superlattices) and its effect on the degree of polarization have not been demonstrated.

Based on the heterojunction model, a semiconductor layer capable of NEA activation on *p*-type GaAs should satisfy two conditions (see Fig. 3.1): (i) the energy difference between the Fermi level and vacuum level should be smaller

than the band gap of GaAs (1.42 eV) to achieve NEA, and (ii) the band gap of activation layer should be greater than that of GaAs to ensure transparency to photons with the GaAs band gap energy. Cs_3Sb has a band gap of 1.6 eV and small electron affinity of 0.45 eV. Such a small electron affinity hints at the possibility of NEA activation on GaAs using Cs_3Sb: as shown in Fig. 3.1, Cs_3Sb satisfies the two conditions mentioned above without any doping control.

Recently, Ref. [5] reported NEA activation of GaAs surfaces with Cs, Sb, and O_2 codeposited layers and changes in photocathode parameters as the thickness was varied. In this work, we demonstrate NEA conditions achieved on bulk *p*-type GaAs with Cs-Sb using various methods of oxygen exposure and its effect on photocathode parameters such as the lifetime, QE, and the degree of spin polarization. Then, a GaAs/GaAsP superlattice sample was activated with one of the methods (codeposition of Cs, Sb, and O_2) and compared with typical Cs-O_2 activation. We find a significant improvement in the lifetime at 780 nm while preserving 90% spin polarization.

3.3 Growth

Samples of 10×10 mm^2 dimension are prepared by cutting highly *p*-doped (Zn 5×10^{18} cm^{-3}) GaAs (100) wafers in air with a diamond scriber. Samples are then solvent cleaned with isopropanol and rinsed in de-ionized water. Wet-etching was later performed for each sample with 1% HF for 30 s to remove the native oxide layer with minimal surface damage [92, 93]. Samples were finally rinsed again in de-ionized water and then moved into vacuum. The growth chamber has Cs and Sb single filament effusion cells [94] installed under ultra-

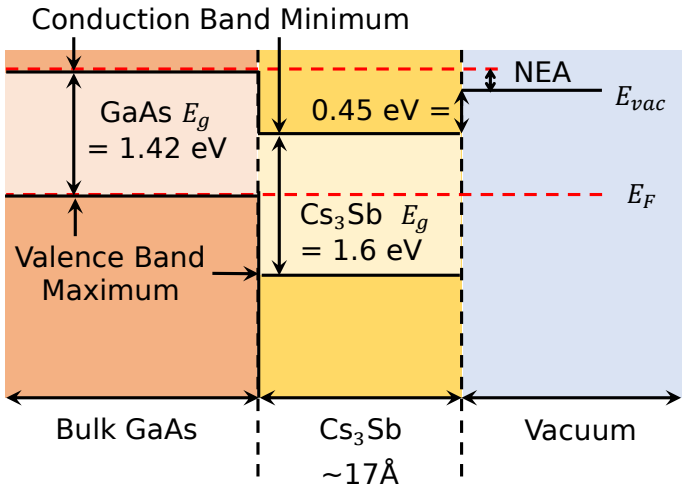

Figure 3.1: Energy band diagram of GaAs activated with Cs_3Sb coating. An alternative activation layer needs to satisfy two conditions to achieve NEA. (i) The energy difference between the vacuum level E_{vac} and Fermi level E_F should be smaller than the GaAs band gap. (ii) The band gap of activation layer should be larger than the GaAs band gap so that the activation layer is transparent for photon energy near the GaAs band gap.

high vacuum (UHV) of $\sim 10^{-9}$ Torr. Shutters in front of each effusion cell act as on/off switches of the flux to the sample surface. A leak valve connected to an oxygen bottle was used to leak oxygen into the chamber during the growths. Total pressure is monitored with a cold cathode gauge. GaAs samples were heat cleaned at ~ 500 °C for about 12 hours. Then temperature was lowered to about 130 °C for the growth. The same heat cleaning procedure was employed to prepare the reference sample, which was later activated with Cs and O_2 at room temperature.

A 780 nm diode laser (~ 10μW) in continuous wave mode was used to excite the samples [95] that were biased at -18 V during the growth. This wavelength is at the NEA GaAs threshold. The drain current was measured via a lock-in amplifier locked to the frequency of an optical chopper used to modulate the

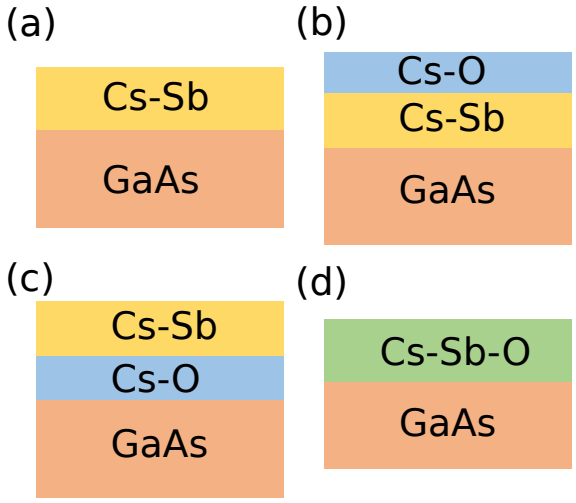

Figure 3.2: Deposition order of different oxygen exposure methods used in Cs-Sb semiconductor activation. (a)-(d) represents methods (a)-(d) in the text.

laser light. Samples were grown with five different methods:

(a) Cs and Sb was codeposited on GaAs without oxygen exposure. This method corresponds to Cs-Sb (purple lines) in Fig. 3.4-3.6.

(b) Cs-O_2 codeposition was additionally performed after Cs-Sb codeposition to study the effect of Cs-O_2 dipole layer on the surface. This method corresponds to Cs-Sb + Cs-O_2 (blue lines) in Fig. 3.4-3.6.

(c) Cs and O_2 was codeposited before the growth Cs-Sb to study the effect of Cs-O_2 dipole layer at the interface between GaAs and Cs-Sb layer. This method corresponds to Cs-O_2 + Cs-Sb (orange lines) in Fig. 3.3-3.6.

(d) Cs and Sb was codeposited under O_2 exposure throughout the growth procedure. This method corresponds to Cs-Sb-O_2 (green lines) in Fig. 3.3-3.7.

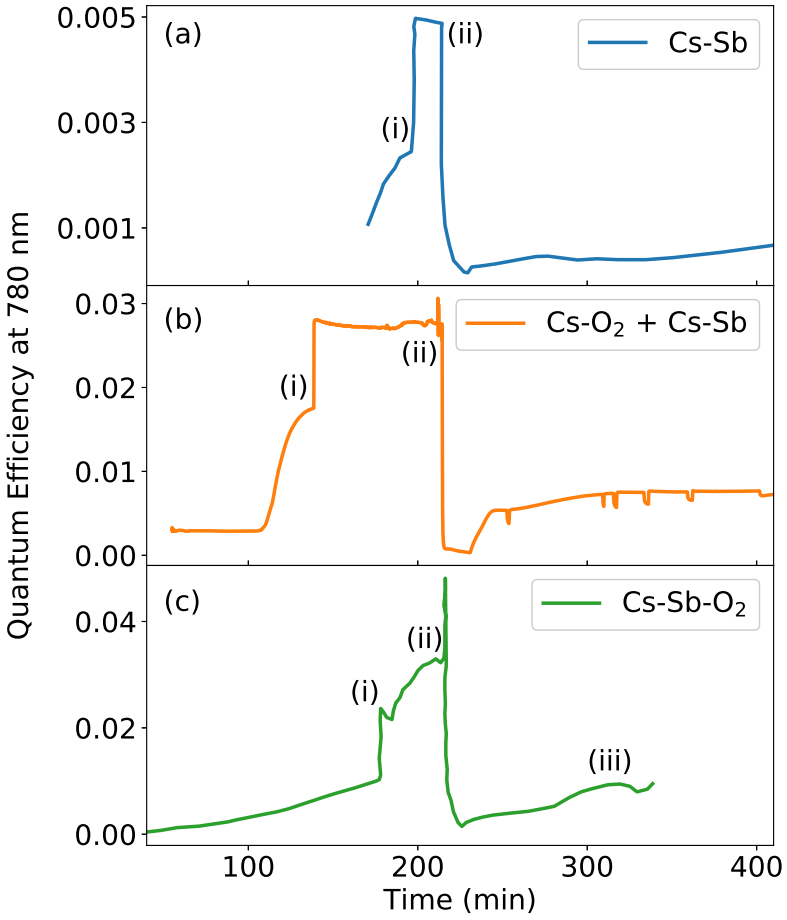

Figure 3.3: Quantum Efficiency of GaAs photocathodes during the thin film growths. The initial QE at 780 nm is not zero due to residual cesium vapor in the growth chamber. The Cs shutter and Sb shutter are opened at (i) and (ii), respectively. (a) Oxygen was not used during the growth (method (a) and (b) in the text). (b) Oxygen was leaked before deposition of Sb (method(c)). (c) Cs, Sb, and O_2 are codeposited during the growths (method (d)). Oxygen leak valve was closed at (iii).

(e) Conventional codeposition of Cs and O_2 was performed for a control sample. This method corresponds to Cs-O_2 (red lines) in Fig. 3.4-3.7.

Figure 3.2 illustrates the layer order for samples grown with Sb.

In Fig. 3.3, the QEs estimated during the different growth procedures of Cs-Sb on bulk GaAs with and without the oxygen exposure are plotted. At the beginning of the growth procedures, we found the samples already photoemitting at 780 nm. We attribute this to the Cs vapors already present in the UHV chamber from previous growth experiments. As the Cs furnace temperature is raised with the shutter closed, the QE increases further, likely because Cs vapors can make it through the gap between the shutter and furnace. In Fig. 3.3, (i) indicates the opening of the Cs shutter and (ii) is when the Sb shutter is opened. For all methods, the Sb shutter was left opened for 1000 seconds to deposit 0.25 nm with a flux of 8.3×10^{11} atoms/cm^2/s, estimated from frequency shifts of a quartz crystal microbalance. Assuming Cs_3Sb single crystal structure, this amount of Sb corresponds to the total film thickness of 1.7 nm [96]. The Cs shutter was left open during the Sb layer deposition and the final cooling of the sample down to 50°C. The photocurrent showed a sudden increase as the Cs shutter is opened and rapid decrease when Sb shutter is opened. For the samples of Fig. 3.3 (a), no oxygen was leaked into the growth chamber (methods (a) and (b)). Oxygen was supplied with a partial pressure of $\sim 5\times10^{-9}$ Torr in Fig. 3.3 (b) and (c); the leak valve was closed just before opening the Sb shutter in (b) (method (c)) and during cooling down (iii) in (c) (method (d)). The sample activated with method (b) was moved under UHV into another chamber (with a base pressure of $\sim 5\times10^{-11}$ Torr) to be further activated by exposing simultaneously to Cs and O_2 at room temperature. For the superlattice sample, Cs, Sb, and O_2 are codeposited for

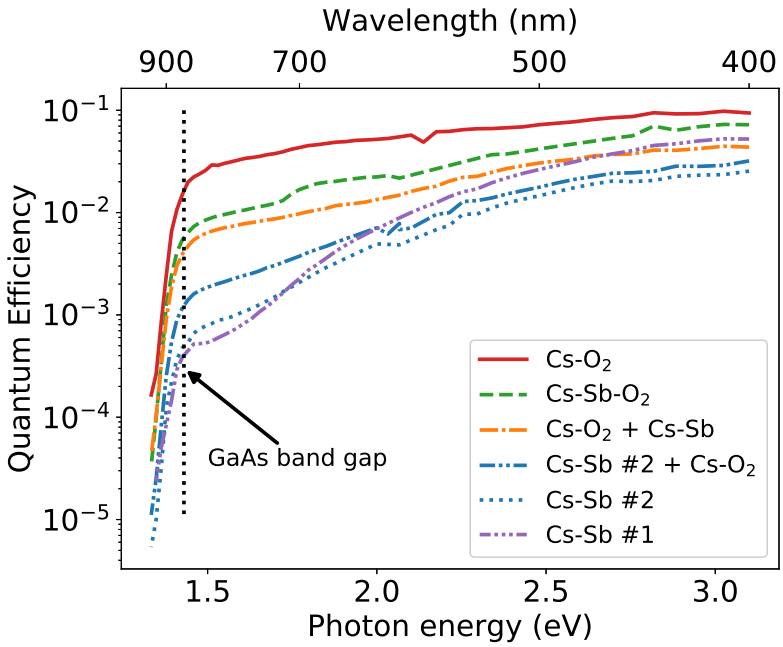

Figure 3.4: Spectral response of GaAs samples activated by Cs, Sb, and O_2 using different methods. All samples indicate NEA activation on the surface by photoemission at GaAs band gap energy (1.42 eV).

activation as in Fig. 3.3 (c). Half the amount of Sb was deposited compared to the bulk samples (0.125 nm Sb and 0.85 nm total thickness) to maintain the spin polarization [5].

3.4 Results

The spectral response of samples with different growth methods are reported in Fig. 3.4. Photoemission at the GaAs band gap photon energy (1.42 eV) confirms NEA achievement on the surface for all of the investigated activation methods. The reference sample, activated with Cs and O_2, has the highest QE across the measured spectral range. The sample activated with only Cs-Sb has the lowest

QE in the infrared region (about 2 orders of magnitude lower than the Cs-O_2 activated sample at 780 nm). Exposing to Cs-O_2 after or before the growth of the Cs-Sb layer (methods (b) and (c)) increases the QE near the GaAs bandgap energy: in particular for the sample prepared with method (c), we observed an increase of QE by about an order of magnitude with respect to the bare Cs-Sb activated sample. Finally, the Cs-Sb-O_2 codeposited sample (method (d)) showed the highest QE near the photoemission threshold among Sb-containing samples. These results illustrate the significance of the Cs-O_2 dipole layer in enhancing the NEA at the GaAs interface.

The robustness of the activating layers was compared by measuring the QE degradation over time. The lifetime of a photocathode is defined as the time QE takes to drop by a factor of e, the base of the natural logarithm [55, 4]. Photocurrent was measured continuously in the range of 1 - 100 nA with a 505 nm diode laser ($\sim 20\mu$W) in Fig. 3.5. The lifetimes extracted from these measurements represent a convolution of the QE degradation from chemical poisoning (known as dark lifetime) and ion back-bombardment (known as charge lifetime). A detailed study of dark lifetime and charge extraction lifetime of codeposited samples is reported in Ref. [5].

From the data reported in Fig. 3.5, it can be seen that Sb deposited samples have at least a factor of 2.6 improvement in lifetime compared to the sample activated with Cs and O_2. The longest lifetime (770 h) was observed when bare Cs-Sb is used for activation, but this method yielded the lowest efficiency near the threshold (Fig. 3.4). One order of magnitude increase in lifetime ($\sim$ 300 h) was observed when the samples are exposed to oxygen either after or during Cs-Sb growths. Table 3.1 reports estimated lifetimes at 780 nm. Spectral re-

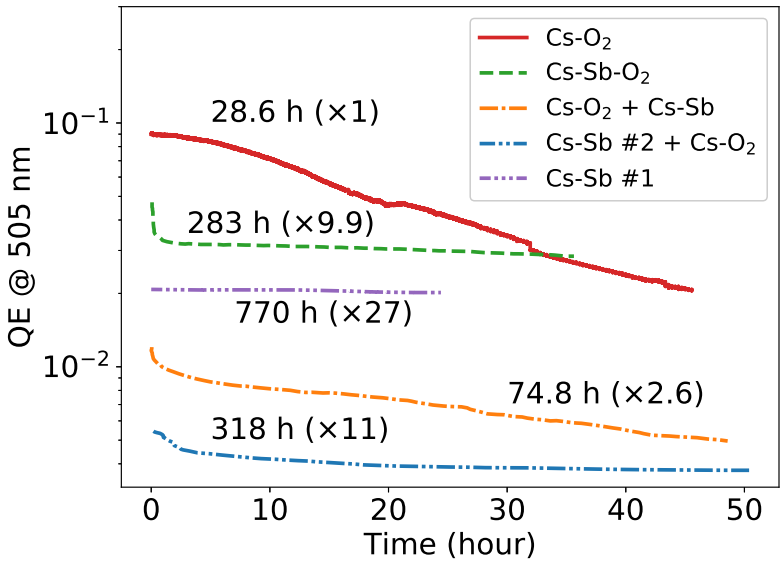

Figure 3.5: Quantum Efficiency degradation as a function of time. 505 nm laser was used to illuminate the sample. The number next to each curve is the lifetime calculated by fitting each curve to an exponential function. Improvement factors from the standard Cs-O_2 activation are in the parentheses.

sponse at 780 nm was measured before and after the QE degradation measurement in Fig. 3.5, and the lifetime is calculated assuming an exponential decrease as a function of time between the two measured points. The Cs-Sb-O_2 activation showed the greatest improvement from Cs-O_2 activation by a factor of 6.8. As opposed to Cs_2Te activation, which showed a rapid increase of the work function as a function of time [64], the Cs-Sb-O_2 layer achieves significant enhancement in lifetime near the photoemission threshold.

Spin polarization of photoemitted electrons was measured by the Mott polarimeter described in Refs. [80, 55]. Monochromatic light was used to produce circularly polarized light directed at normal incidence to the sample surface. Longitudinally spin-polarized electrons were bent 90° by electrostatic lenses and Mott scattered with 20 keV at a tungsten target, which was calibrated to

Activation method	Initial QE at 780 nm	Final QE at 780 nm	Lifetime estimate (hour)	Improvement factor
$Cs\text{-}O_2$	3.3×10^{-2}	1.4×10^{-3}	15	×1
$Cs\text{-}O_2$ + Cs-Sb	9.5×10^{-3}	2.9×10^{-3}	41	×2.7
Cs-Sb + $Cs\text{-}O_2$	3.8×10^{-3}	1.1×10^{-3}	70	×4.6
$Cs\text{-}Sb\text{-}O_2$	1.0×10^{-2}	7.0×10^{-3}	104	×6.8

Table 3.1: Lifetimes at 780 nm estimated by comparing initial QE and final QE after the QE degradation measurement in Fig. 3.5.

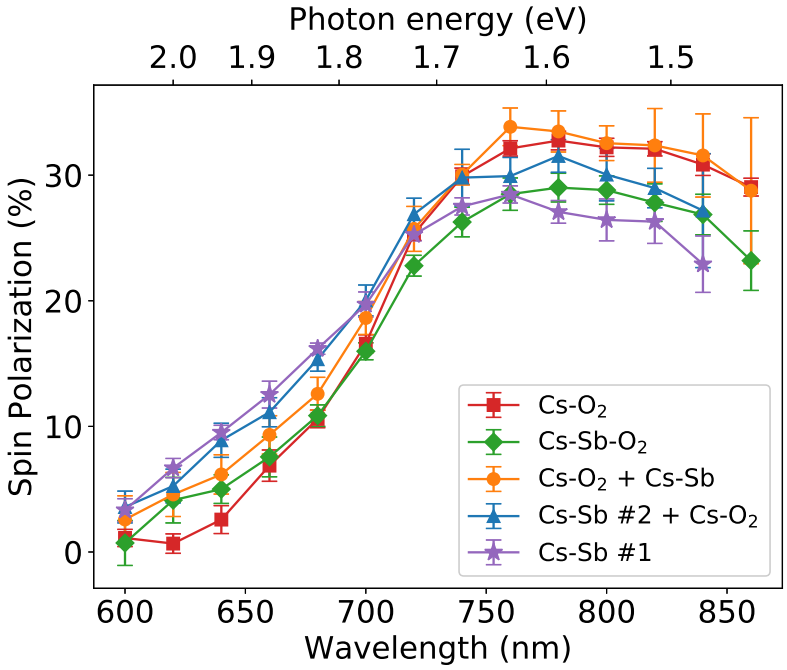

Figure 3.6: Spin polarization of photoemitted electron from GaAs activated by Cs, Sb, and O_2.

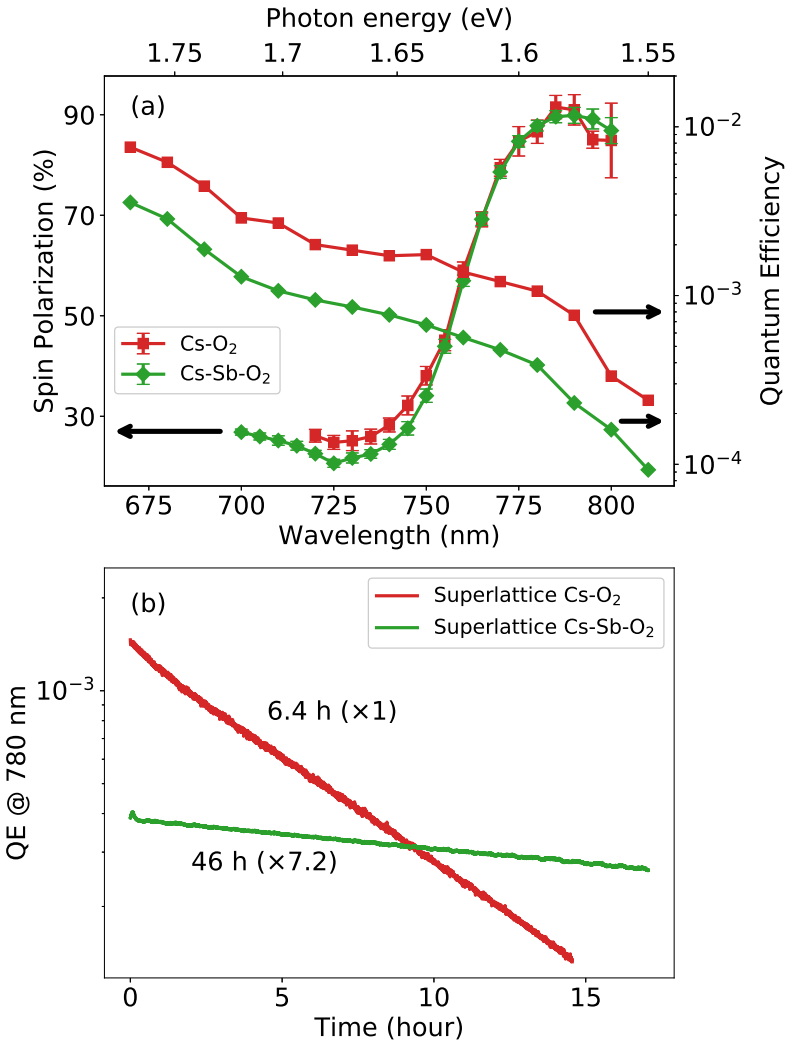

Figure 3.7: Spin polarization, quantum efficiency, and lifetime measurement of GaAs/GaAsP superlattice sample activated by codeposition of Cs-Sb-O_2 and standard Cs-O_2. The numbers in the parentheses are lifetime improvement factors from the standard Cs-O_2 activation.

have a Sherman function of 0.18 [80, 55]. Photoelectron spin polarization was measured as a function of wavelength for each sample (Fig. 3.6). The maximum spin polarization varied up to 5%, which corresponds to about 3 standard deviations. The detailed study [5] on the samples activated with the Cs-Sb-O_2 method reveals a significant spin depolarization as thickness of the Sb layer grows.

Since the Cs-Sb-O_2 codeposited sample showed both the highest QE at the photoemission threshold among Sb deposited samples and a significantly improved lifetime, we chose the codeposition method to activate a GaAs/GaAsP superlattice sample [97] (Fig. 3.7). Compared to the bulk samples, a half the amount of Sb is deposited (0.125 nm) to minimize depolarization at the activation layer [5]. Both samples showed ~ 90 % maximum spin polarization with agreement within one standard deviation. The QE at 780 nm was a factor of 3 smaller for the semiconductor activated sample. QE was continuously measured in Fig. 3.7 (b) for lifetime estimation at 780 nm, the wavelength commonly used for a highly spin polarized photoemission. The lifetime showed a factor of 7 improvement, which is similar to the bulk results in Table. 3.1 that were activated with twice the amount of Sb.

3.5 Discussion

The sample prepared with method (c) (where the Cs-O_2 is deposited on the surface of GaAs under the Cs-Sb layer) has a higher QE than the sample prepared with method (b), where the Cs-O_2 is deposited above the Cs-Sb layer. This suggests that despite the small thickness of the activating layers, segregation can take place such that the intermediate Cs-O_2 layer retains the strong electric dipole enhancing the transmission from GaAs into the Cs-Sb layer. Additionally, the QE near threshold of the sample exposed to Cs-O_2 after depositing Cs-Sb is larger than the one activated only with Cs-Sb. Studies on the nature of the GaAs/Cs-O activation layer indicate that the dipole layer consists of a Cs^+-O^{2-}-Cs^+ sandwich on a O-GaAs layer, and the strong double dipole layer results in a higher QE compared to Cs-only activation [89]. On the other hand, studies

on the oxidation of alkali antimonide photocathodes show that, during oxidation, the films segregate in a alkali-oxide rich surface layer on top of the alkali antimonide layer [98]. In particular, at low oxygen exposures (less than 10 L for $Cs_{2.5}K_{0.5}Sb$) [98], the top surface is mainly composed of a Cs suboxide ($Cs_{11}O_3$) [99] that is known to promote photoemission, in particular at long wavelengths [100].

The above discussion suggests that the sample activated with Cs-Sb-O_2 should indeed have the the largest QE among the alternative methods. In this case, the continuous oxygen exposure can result in the formation of a strong electric dipole at both the interface with GaAs and at the surface of Cs-Sb that can favor both electron tunneling from GaAs to Cs-Sb and electron emission from Cs-Sb to vacuum. The oxygen dosed on the samples during codeposition can be estimated to be of the order of 50 L - 75 L; since Cs is provided during the oxygen exposure and after the closure of the oxygen leak valve, it is reasonable to expect the formation of Cs-rich suboxides on the sample surface.

Photoexcited electrons experience a potential barrier at the GaAs surface in the process of emission into the vacuum. Although various models of the potential barrier were proposed, fundamental understanding of the nature of the barrier is lacking [101, 102]. Rectangular [103], triangular [3], and double triangular [102] shapes have been proposed in previous studies to reproduce various experimental observations. In Fig. 3.8, a simple potential barrier was constructed to numerically investigate how different methods of oxygen exposure during Cs-Sb growths can affect the shape of the potential barrier and QE as a result. The transmission probabilities and corresponding quantum efficiencies of various modeled potential barriers were calculated using the propagation matrix

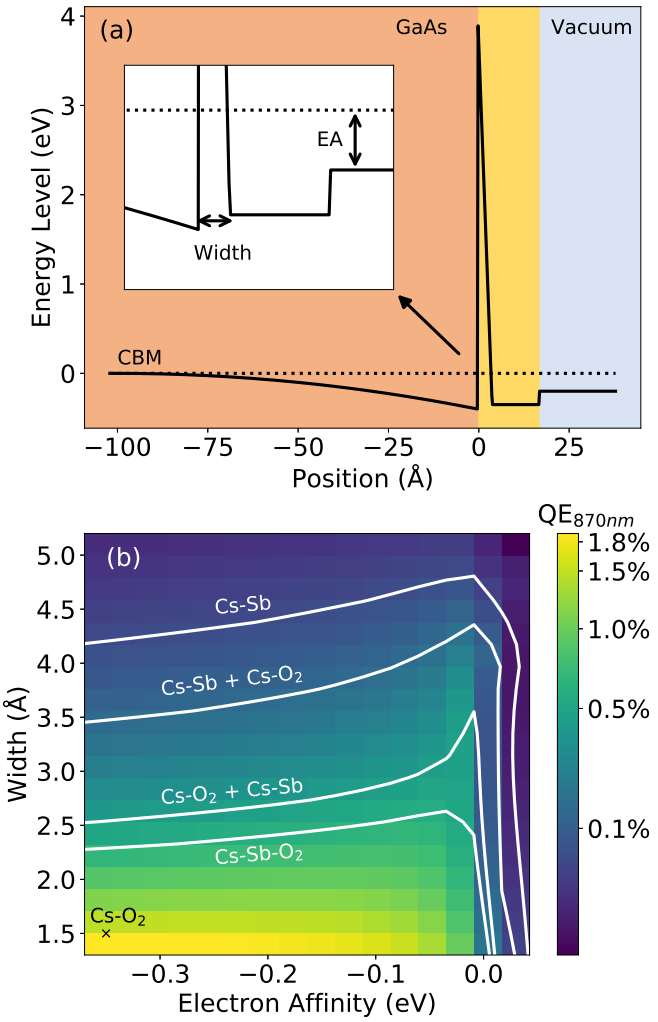

Figure 3.8: Numerical simulation of quantum efficiency under various potential barrier shapes. (a) Potential barriers were constructed for 1.7 nm thick semiconductor activation layer to calculate transmission probabilities. Red, yellow, blue regions correspond to GaAs, activation layer, and vacuum, respectively. An enlarged view of the barrier near the surface is shown in the inset. (b) Width and EA are varied to compute threshold QE. The black mark corresponds to the standard Cs-O_2 activation sample. Potential barrier parameters in Ref. [3] were used. White contour lines are sets of parameters that reproduce experimentally measured QEs.

approach [101, 104, 105].

In the bulk of GaAs, we implement quadratic band-bending near the surface with a 10 nm band bending region and 0.4 eV band bending magnitude [101]. A simple triangular potential barrier was placed at the interface between GaAs and the activation layer. The height of the triangle was fixed at 4 eV above the conduction band minimum (CBM) of GaAs [3] while the width was varied throughout the simulations. The variation of the width can be interpreted as a change in dipole moment strength at the interface. The bottom of the potential well between the triangular barrier and the vacuum interface was fixed at 0.35 eV below the conduction band minimum [106, 102, 107]. The vacuum interface is positioned at 1.7 nm from the GaAs surface, which is the estimated thickness of the activation layer.

Based on the transmission probabilities (P) calculated by the propagation matrix approach [104, 105], corresponding quantum efficiencies (QE) are computed numerically with the following equation:

$$\mathrm{QE} = (1 - R)F \frac{\int_0^\infty dE\, f(E) \int_0^1 d(\cos\theta) P(E\cos^2\theta)}{\int_0^\infty dE\, f(E) \int_{-1}^1 d(\cos\theta)}. \tag{3.1}$$

Here, R is the optical reflectance of GaAs, F is a scattering contribution (from holes, impurities, and phonons) [101] which can be approximated to be independent of energy near the photoemission threshold [7], θ is the angle between the electron velocity and the surface normal, and $f(E)$ is a Fermi-Dirac distribution of photoexcited electrons:

$$f(E) = \frac{1}{1 + e^{[E-(h\nu - E_g)]/kT}}, \tag{3.2}$$

where $h\nu$ is the photon energy, E_g is the GaAs band gap, k is the Boltzmann constant, and T is the room temperature. Additional scatterings at the semicon-

ductor activation layer can be considered to be mostly elastic electron-electron collisions, so they have been ignored [5].

In Fig. 3.8 (b), QEs are calculated for various sets of the triangle width and electron affinity. The photoemission threshold wavelength 870 nm was used, and the scattering term F was set to be 0.21 to match the experimentally measured value of Cs-O_2 activated sample to the calculated one. The width of triangular potential barrier of Cs-O_2 activation layer is reported to be 0.15 nm [3] with 0.35 eV NEA [102, 107, 106]. The white contour line for each growth method represent the set of parameters that reproduce the experimentally measured QE at 870 nm. The contour lines suggest that when NEA is greater than 0.1 eV, the efficiency is roughly independent of NEA while the barrier width plays a critical role in determining QE. Considering that a small width represents a strong dipole moment at the surface, activation with oxygen at the interface between bulk GaAs and the activation layer is essential to achieve a high QE. Thus, this simple model can explain why samples activated with oxygen before and during the Cs-Sb growth showed greater improvement in QE compared to the sample exposed to oxygen after Sb deposition, which is related to greater NEA at the vacuum interface.

3.6 Conclusion

We have investigated the NEA activation of GaAs samples with Cs, Sb and O_2 in various recipes. Of the recipes attempted, we found that the codeposition method can achieve the highest QE ($\sim$ 1% at 780 nm) with a factor of 10 and 7 improvement in lifetime at 505 nm and 780 nm, respectively, compared to the

conventional Cs-O_2 activation. Similar results were obtained for the high polarization GaAs/GaAsP superlattice sample. This sample showed a factor of 7 improvement in lifetime at 780 nm without any depolarization at a cost of a factor of 3 smaller QE. A simple numerical model was proposed to estimate QE for various shapes of the potential barrier at the relatively thick semiconductor activation layer. According to the model, the dipole moment strength at the GaAs interface with the activation layer is critical to achieve a high QE at the photoemission threshold. This explains the significant improvement in QE we observed when the samples were exposed to oxygen before activation layer growths.

Future work will involve surface characterization of the activation layer to understand the chemical and structural composition. This information can be used to properly model the heterojunction band structures with density functional theory. Monte Carlo techniques can be considered to model the electron spin transport and to study the depolarization mechanisms. Furthermore (and perhaps most critically), we plan to test the performance of these unconventional activation layers in a real high voltage, high current DC gun environment in the future. In this environment, one can perform lifetime studies in broader ranges of laser power and extraction current.

3.7 Acknowledgments

This work was supported by the Department of Energy under Grant No. DE-SC0019122 and National Science Foundation under Grant No. PHY-1549132, the Center for Bright Beams. Authors would like to acknowledge Marcy Stutzman,

Matt Poelker, Joe Grames, and William DeBenedetti for valuable discussions, help in preparing GaAs samples, and providing GaAs/GaAsP superlattice samples.

4

Operation of Cs-Sb-O activated GaAs in a high voltage DC electron gun at high average current

This chapter is planned to be submitted for publication in the Journal of Applied Physics.

4.1 Abstract

Negative Electron Affinity (NEA) activated GaAs photocathodes are the most popular option for generating a high current (> 1 mA) spin-polarized electron beam. Despite its popularity, a short operational lifetime is the main drawback of this material. Recent works have shown that the lifetime can be improved by using a robust Cs-Sb-O NEA layer with minimal adverse effects. In this work, we operate GaAs photocathodes with this new activation method in a high voltage environment to extract a high current. We observed spectral dependence on the lifetime improvement. In particular, we saw a 45% increase in the lifetime at 780 nm for Cs-Sb-O activated GaAs compared to Cs-O activated GaAs.

4.2 Introduction

An electron source capable of sustaining high-intensity production of spin-polarized electrons is highly desired for nuclear and high energy physics applications [88, 108]. Furthermore, electron microscopy technologies can utilize spin-polarized electrons to study magnetization in materials and nanostructures [86, 17, 87]. A Negative Electron Affinity (NEA) activated GaAs in a high voltage electron gun is the only viable option to produce a highly spin-polarized electron beam at a high current. However, the extreme vacuum sensitivity of the NEA layer is the main drawback that results in rapid Quantum Efficiency (QE) degradation over time; hence it has a short operational lifetime compared to other types of photocathodes [4, 55, 66, 5].

Quantum mechanical selection rules in optically stimulated electronic transition must be leveraged to achieve the photoemission of spin-polarized electrons from bulk GaAs [44, 1]. Using circularly polarized light with photon energy slightly larger than the bandgap, electrons can be excited from the top of the valence band to the bottom of the conduction band with polarization up to a theoretical limit of 50% [44]. Extracting these electrons from the photocathode requires a vacuum interface with NEA condition. As in bulk GaAs, most layered GaAs-based photocathodes can be designed to achieve a sufficiently large QE and high electron spin polarization when excited with wavelengths close to 780 nm [52]. Therefore, the operational lifetime at 780 nm is crucial for large accelerator facilities applications.

Three main mechanisms are responsible for the rapid degradation of QE: ion back-bombardment [4, 74, 109], chemical poisoning [56], and thermal des-

orption of the activation layer [57]. Ion back-bombardment occurs when the electron beam ionizes the residual gases in the vacuum. The positively charged ions are accelerated towards the cathode and degrade the cathode performance [4, 74]. Chemical poisoning of the cathode happens as the NEA activation layer chemically reacts with the residual gases in the vacuum [56]. As ion back-bombardment and chemical poisoning degrade the QE during beam operation, a higher laser intensity is required to maintain the beam current at the same level, and the increased laser power might further accelerate the thermal desorption of the NEA layer. Among the three mechanisms, the ion back-bombardment is considered the most significant contributor to performance degradation during high current operations. It has been shown that such a process can be minimized by extracting electrons a few mm off from the electrostatic center, limiting the photocathode active area, increasing the laser spot size, and applying a positive bias to the anode [4, 110].

Ion back bombardment can degrade QE by three different processes. High energy ions ($\gtrsim$ 5 keV) can interact with lattice atoms and create vacancies, directly damaging the GaAs structure [111, 109]. Lower energy ions ($\lesssim$ 500 eV) can penetrate the cathode surface and create interstitial defects near the vacuum interface. These defects will affect the diffusion length of electrons and hence lower the escape probability of photoelectrons [109]. The last possibility is that ions between 500 eV and 5 keV can interact with atoms on the surface and remove the NEA activation layer via sputtering [111]. The QE degradation is expected to be a convolution of these three processes, but the relative contribution of each is not well understood and left to be explored. Understanding the convolution would be critical to potential mitigation.

Traditional NEA activation layers such as Cs-O_2 and Cs-NF_3 form a sub-monolayer that is chemically reactive and weakly bound to the surface [57, 56]. A study found that using two alkali species, Cs and Li, for NEA activation could improve the chemical stability of GaAs photocathode under CO_2 exposure [77, 76, 90]. Recently, multiple research groups reported significantly improved lifetime using a few nm thick semiconductor activation layer with elements that form more robust photocathodes, such as Cs, Sb, Te, O [112, 113, 114]. We reported a factor of 5 improvements in charge lifetime at 532 nm wavelength with Cs-Te activation layer [55] and a factor of 7 improvements at 780 nm with Cs-Sb-O layer [66]. Moreover, these layers showed a minimal adverse effect on spin-polarization [55, 66, 5]. However, these photoemission measurements were done with a 10's of eV bias and 100's of nA beam current, which is significantly different from the harsh environment of an electron gun that operates on the scale of 100's of keV. Specifically, the amount of current extracted and the energy-dependent residual gas ionization cross-sections are orders of magnitude different [4]. Furthermore, the primary QE degradation mechanism was chemical poisoning in our previous works as opposed to ion back bombardment [5]. In this work, we operated Cs-Sb-O and Cs-O activated GaAs photocathodes in the High ElectRon Average Current for Lifetime ExperimentS (HERACLES) beamline at Cornell University in order to make a direct comparison of their performance at 200 keV beam energy at 1 mA average current.

4.3 Growth

Highly p-doped (Zn 5×10^{18} cm^{-3}) GaAs (100) wafers were cleaved in air with a diamond scribe. Cleaved samples were rinsed in de-ionized water and solvent

cleaned with isopropanol. We performed wet-etching with 1% HF acid for 30 s, and then the samples were loaded into the vacuum for heat cleaning at ~ 500 C$^\circ$ for ~ 48 hours. Cs-O activation was performed in a vacuum chamber directly connected to the back of the electron gun that has a pressure of $\sim 10^{-10}$ Torr. Resistively heated dispensers from SAES Getters were used for the Cs source, and O_2 was injected with a mechanical leak valve. We activated GaAs samples with the Cs-O_2 codeposition method at room temperature.

For Cs-Sb-O activation, the growth was performed in a separate vacuum system located in another laboratory, and the cathodes were subsequently transported with a vacuum suitcase. The growth chamber has a pressure of $\sim 10^{-9}$ Torr, and single filament effusion cells were installed as Cs and Sb sources. Shutters in front of each source act as an on/off control of the flux. We leaked O_2 into the chamber with a mechanical leak valve similar to the Cs-O activation chamber. The temperature of the samples was kept at ~ 130 C$^\circ$ during the growth. QE at 780 nm was monitored during the growth with a diode laser (~ 10 μW) under 18 V negative bias.[95] Fig. 4.1 demonstrates the QE at 780 nm during the growth process. (i) Samples were initially activated with just Cs until QE peaks and started decreasing. (ii) As soon as the QE decrease was observed, O_2 was leaked into the chamber. (iii) the Sb shutter was opened when QE saturated to a percent level. Cs, Sb, and O_2 are all being deposited simultaneously during Sb deposition. (iv) Sb shutter was closed after depositing 0.2 nm. The heater was turned off, the O_2 leak valve was closed, and the Cs shutter was closed soon after. The Sb deposition amount and flux (5×10^{11} atoms/cm^2/s) were estimated using a quartz crystal microbalance. The decreased QE during Sb deposition recovered while cooling down of the sample. The activated cathodes were transported to the gun using a custom ultrahigh vacuum suit-

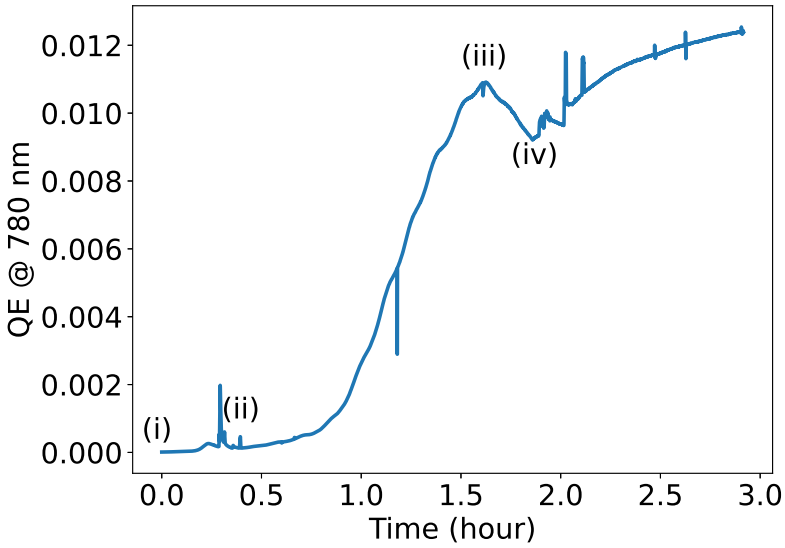

Figure 4.1: Quantum Efficiency at 780 nm of GaAs photocathode during Cs-Sb-O activation. Cs shutter was opened at (i), and the O_2 leak valve was opened at (ii). Sb shutter was opened at (iii) and closed at (iv).

case that has a base pressure of $< 10^{-10}$ Torr [115]. The suitcase was constantly pumped by a compact 400 l/s non-evaporative getter during the transport, and an 8 l/s ion pump was turned on once it was attached to the load-lock chamber of HERACLES. We typically pumped the load-lock chamber overnight before transporting the cathodes into the gun.

4.4 Instrument

The HERACLES beamline consists of a 400 keV electron gun and a 75 kW beam dump (See Fig. 4.2). The gun was originally fabricated for the Cornell Electron Recovery Linac (ERL) program. It was used to demonstrate the record highest average current obtained from a photocathode [116]. Recently, the gun, beam dump, and some of the beamline components were moved to the same build-

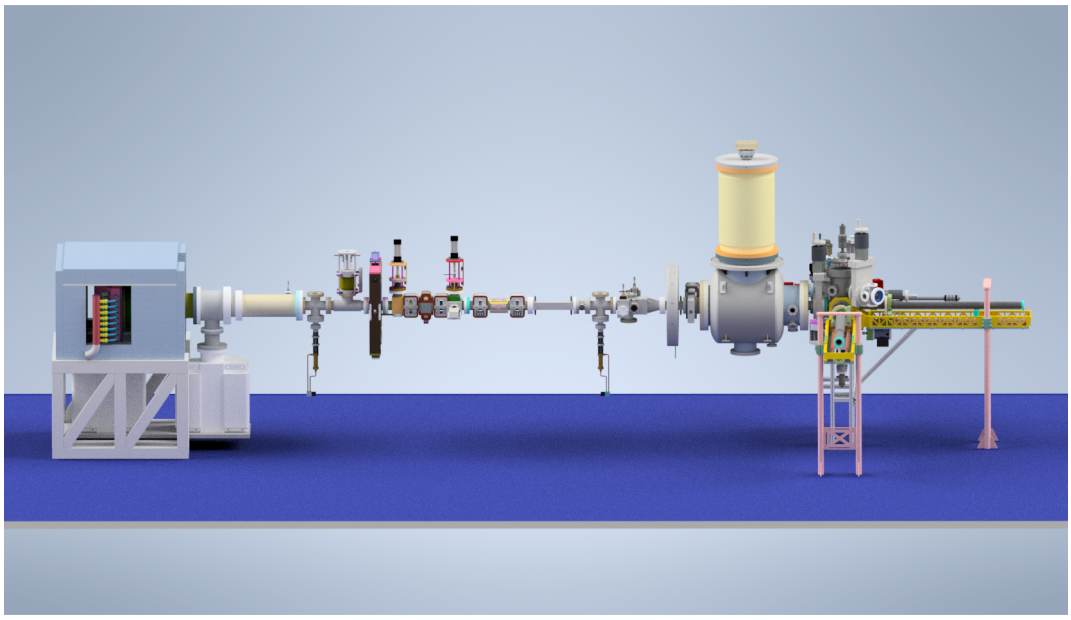

Figure 4.2: HERACLES beamline. Eletron beam travels from right to left. The beamline is consisted of two solenoids, three horizontal/vertical corrector pairs, three view screens, a faraday cup, and a quadrant detector.

ing as the Cornell Photocathode laboratory to enable an experimental program for producing and testing long-lived photocathodes at high average beam currents. In the current configuration, beyond the gun, the HERACLES beamline comprises two solenoids, three horizontal/vertical corrector pairs, three BeO pneumatically mounted view screens, a faraday cup for low current (~100 nA) measurements, an emittance measuring system, and a quadrant detector for beam position monitoring at high currents. The beam dump is composed of 16 chilled water lines that are independently monitored with thermocouples that serve as a further diagnostic during high-current running. The beamline also includes two sets of clearing electrodes to reduce ion-back bombardment.

During the high current runs presented in this work, we used Sabre Innova Argon gas laser by Coherent operated in the visible at 488 nm. A 1-to-1 imaging

system consisting of a single 750 mm lens is used to image a 1.2 mm diameter pinhole onto the cathode active area. A small portion of the laser light is split off into a diagnostics optics path to allow the power to be monitored during the run. The laser spot was positioned on the 7 mm off-centered active area on the cathode that has 4 mm diameter (see Fig. 4.3 (a)). Our control system is EPICS-based [117]. For running at 100 μA or more, the beam current is inferred from the current drawn by the gun power supply. During a charge lifetime measurement, the laser power is adjusted to maintain a constant current via a proportional-integral feedback loop implemented in Python with PYEPICS.

Two vacuum chambers are connected behind the HERACLES gun. The first chamber has a mechanical arm for placing and removing cathodes in the gun, a vacuum attachment port for accepting cathodes via a vacuum suitcase, and has the capacity to store up to three cathodes. The second chamber, dubbed the QE-mapping chamber, has a cesium source and oxygen leak valve to enable Cs-O activation of GaAs. In this chamber, the saddle is electrically isolated and can be negatively biased to allow for photocurrent to be monitored during an activation. Outside this chamber, a diode laser is mounted to a 2D motorized stage to obtain transverse maps of the cathode's QE (Fig. 4.5). Such a diagnostic is critical for an examination of the cathode after a high-current run to identify the main driver(s) of the cathode's performance degradation.

4.5 Results and Discussion

Charge lifetime is defined as the amount of charge extracted until QE drops to $1/e$ of the initial value [4, 55]. In Fig. 4.4, QE at 488 nm was monitored during

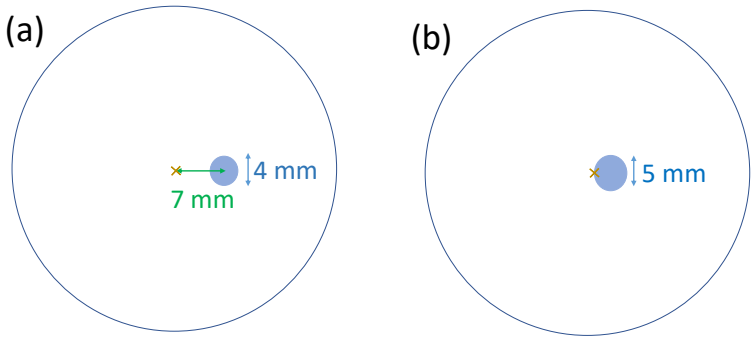

Figure 4.3: Active area (blue shaded area) geometry relative to the electrostatic center of the gun (yellow cross). (a) At Cornell DC electron gun, the active area is 7 mm off from the center. (b) At Jefferson Lab DC gun, the active area is closer to the electrostatic center [4].

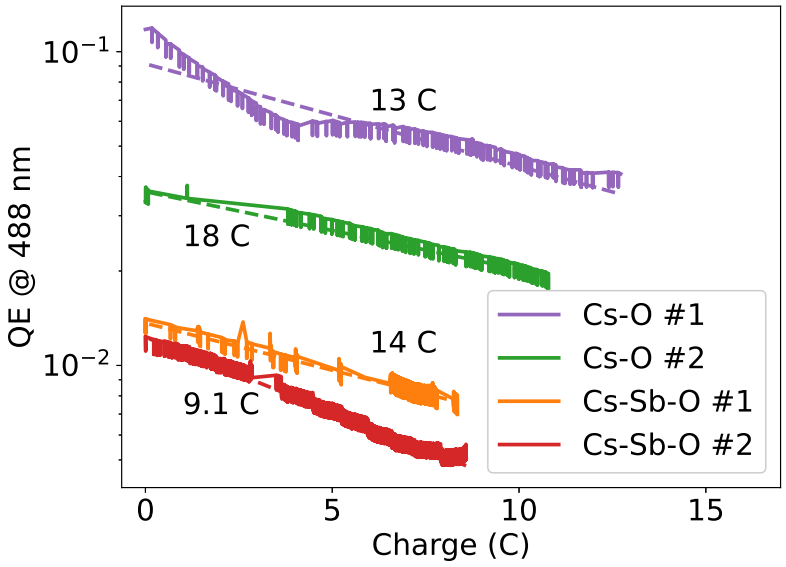

Figure 4.4: Quantum Efficiency degradation during 200 kV DC electron gun operation. 488 nm Laser was used to extract 1 mA of current. The solid lines represent measured data, while the dashed lines are exponential fits to the solid lines. The numbers next to each curve are estimated charge lifetimes from the exponential fit functions.

200 keV operation at 1 mA. We obtained charge lifetimes around 15 C for the reference Cs-O activated GaAs photocathodes. It must be noted that this value is two orders of magnitude lower than the ones achieved at the Thomas-Jefferson lab [4]. We believe there are two main reasons. First, the pressure of the DC gun at Cornell is typically around $\sim 2 \times 10^{-11}$ Torr in a standby mode, and it can rise up to 10^{-10} Torr during an operation. On the other hand, the electron gun in the Jefferson Lab is operated under mid 10^{-12} Torr pressure [4]. Secondly, it has been found that a high voltage photogun can produce unwanted photoelectrons from the edge of an active area that is not properly transported away [4, 78]. These electrons follow extreme trajectories and strike the anode or beam pipe wall, resulting in vacuum degradation and, consequently, QE loss due to increased rates of vacuum poisoning and ion-bombardment. Jefferson lab showed improvements in charge lifetime by limiting the size of the active area to 5 mm and positioning the active area near the electrostatic center [4]. They achieved the largest charge lifetime when the laser spot was positioned at the furthest spot of the active area (5 mm). A comparison of the active area geometry is demonstrated in Fig. 4.3. Although our active area has a similar size to that of the Jefferson Lab, the active area is far off from the center and can cause vacuum and QE degradation. When the active area has a 12.8 mm diameter size positioned near the electrostatic center, the Jefferson Lab was able to achieve only 10's of C for charge lifetime [4]. Considering the geometry, 15 C of charge lifetime agrees with measurements from the Jefferson Lab within an order of magnitude. This agreement suggests that the HERACLES beamline is appropriate to perform comparison studies between the standard activated GaAs and Cs-Sb-O activated GaAs.

In Fig. 4.4, we report the QE at 488 nm as a function of extracted charge mea-

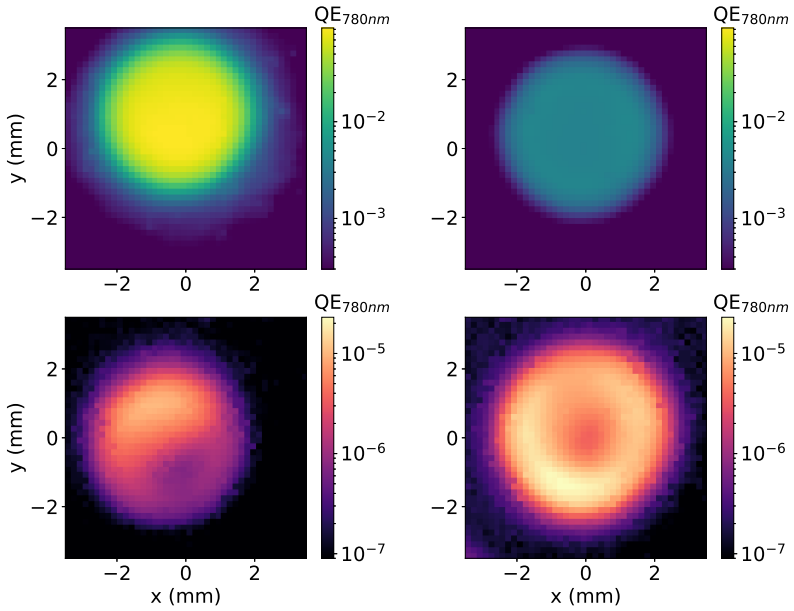

Figure 4.5: Quantum Efficiency map of active areas. 780 nm diode laser was used. The left images are Cs-O activated GaAs, while the right images are Cs-Sb-O activated GaAs. The top images were taken before the gun operation, and the bottom images were taken after.

surements for two Cs-Sb-O activated samples and two Cs-O activated samples. The initial QE of Cs-Sb-O activated samples are smaller compared to the standard Cs-O activated samples for two reasons. First, in our previous works, we observed roughly a factor 2-3 smaller QE when Sb was used during the activation procedure [5]. Secondly, the growths of Cs-Sb-O activated GaAs were done in a separate chamber, and the transport was done with a vacuum suitcase. This transport process takes about 24 hours, and we observed that the QE decreased by a factor of 3 after the transport was completed. On the other hand, the standard Cs-O activations are done in an attached chamber to the electron gun, and the samples were operated soon after the growths. Regardless of the initial QE, the charge lifetimes of both activation methods agreed within a factor of 2. Because of the smaller QE, the average laser intensity during the Cs-Sb-O

runs was necessarily higher, and, consequently, the rate of thermal desorption was faster. Based on the thermal analysis found in reference [57], the temperature of the GaAs would have increased by a few Kelvin at most during the run. This same paper reports a few degree temperature rise has a negligible impact on the dark lifetime of GaAs activated with Cs-O. If we assume Cs-Sb-O to be equally robust to temperature, it is unlikely the lower QE impacted our lifetime measurements.

In the photocathode community, the stability of the NEA layer has been thought to be the main reason for the short operational lifetime of GaAs photocathodes [109, 111]. Therefore, one might expect that an enhancement of the chemical robustness of the NEA layer would translate into an improved charge lifetime at high-current operation. However, we were unable to directly observe an improvement in charge lifetime in our measurements at 488 nm despite a more robust NEA layer. In particular, the charge lifetime at 488 nm for Cs-Sb-O activated sample #2 was worse by 30 % (9.1 C) compared to that of the Cs-O activated sample #1 (13 C). Postmortem QE maps were obtained with 780 nm light for these two samples in Fig. 4.5. The QE map demonstrates non-uniform damage on the surface, indicating that high current beam extraction caused the damage as opposed to vacuum poisoning, which we would expect to be uniform. Unlike the 488 nm wavelength case, we measured a higher final QE at 780 nm for Cs-Sb-O activated sample at the damaged area (3.8×10^{-6}) compared to that of the Cs-O activated sample (7.1×10^{-7}) despite one order of magnitude lower initial QE. This suggests that the Cs-Sb-O layer formed a more robust NEA layer in terms of chemical stability. Although the charge lifetime at 780 nm was not measured directly, based on the amount of charge extracted during operation (Q_{tot}) and the initial and final QE ($QE_{i,f}$), we can estimate the charge

Activation method	Initial QE at 780 nm	Final QE at 780 nm	Extracted charge (C)	Lifetime at 780 nm (C)
Cs-O_2 #1	9.1×10^{-2}	7.1×10^{-7}	13	1.1
Cs-O_2 #2	4.6×10^{-2}	2.1×10^{-6}	11	1.1
Cs-Sb-O #1	4.2×10^{-3}	5.2×10^{-5}	8.4	1.9
Cs-Sb-O #2	3.8×10^{-3}	3.8×10^{-6}	8.6	1.3

Table 4.1: Estimated lifetimes at 780 nm based on Eq. 4.1.

lifetime at 780 nm (τ_c) by assuming an exponential decay:

$$\begin{aligned} \mathrm{QE}_f &= \mathrm{QE}_i \, e^{-Q_{tot}/\tau_c} \\ \therefore \tau_c &= \frac{Q_{tot}}{\log(\mathrm{QE}_i/\mathrm{QE}_f)}. \end{aligned} \tag{4.1}$$

In Table 4.1, the charge lifetimes at 780 nm are estimated for the four samples. The estimated charge lifetime at 780 nm is 1.6 ± 0.4 C for Cs-Sb-O activated GaAs and 1.1 ± 0.1 C for Cs-O activated GaAs.

This paragraph attempts to qualitatively explain the spectral dependence of lifetime improvement based on spectral response measurements we performed in previous work [5, 66]. Assuming the QE degradation is mainly due to damage done to the NEA layer, we can model the spectral response to simply shift horizontally during beam operation because of the increased work function. Based on this assumption, estimated shifts in spectral response (QE(λ)) are plotted in Fig. 4.6. The solid lines are the spectral response curves of Cs-O activated GaAs and Cs-Sb-O activated GaAs from our previous measurements [5, 66]. The dashed lines have been obtained by simply shifting the same curves along the wavelength axis until the QE at 488 nm corresponds to the estimated QE after a 5 C extraction. Note 5 C is about half of what we extracted in Fig. 4.4. The charge lifetimes at 488 nm in Fig. 4.4 were used (15 C for Cs-O activated

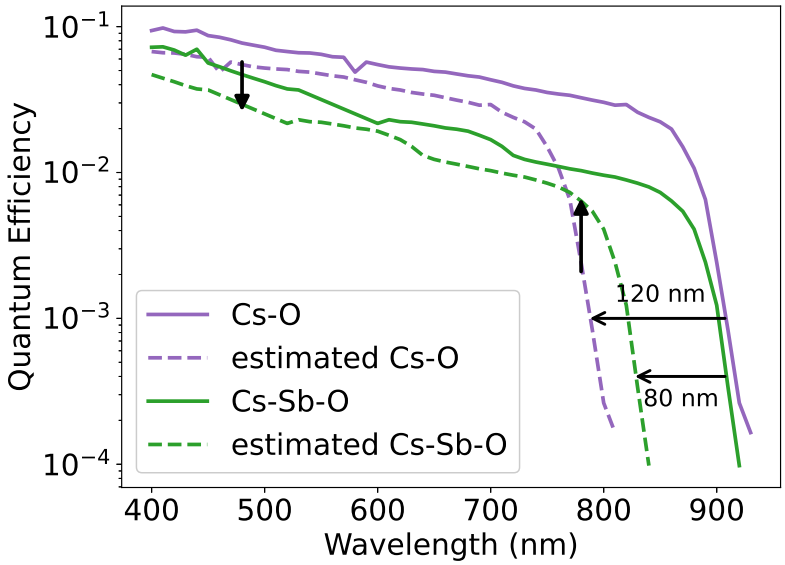

Figure 4.6: Estimated shifts in spectral response due to surface damage. The solid lines are typical spectral responses of Cs-O activated GaAs and Cs-Sb-O activated GaAs from our previous work [5]. The dashed lines are estimated spectral responses of damaged cathodes. We assumed 5 C of charge is extracted for both samples. The spectral response shifts were 120 nm for Cs-O activated GaAs and 80 nm for Cs-Sb-O activated GaAs. The vertical black arrows indicate QE differences of damaged cathodes at 488 nm and 780 nm.

GaAs and 12 C for Cs-Sb-O activated GaAs). It is estimated that the spectral response would shift 120 nm for Cs-O activated GaAs and 80 nm for Cs-Sb-O activated GaAs. Despite a shorter lifetime at 488 nm for the Cs-Sb-O layer, the horizontal shift, or the work function increase, was smaller. This is because the log slope of spectral response ($d\log(\mathrm{QE})/d\lambda$) at 488 nm was steeper for Cs-Sb-O activated sample (6.4×10^{-3}/nm) compared to that of Cs-O activated sample (2.8×10^{-3}/nm). In other words, the sensitivity of the work function is the culprit for the shorter lifetime at 488 nm of the Cs-Sb-O activated sample, but the work function increase itself was smaller. Since the work function increased less due to the robust NEA layer, the final QE at 780 nm was greater than that of the

standard activated GaAs.

4.6 Conclusion

In this work, we operated Cs-O and Cs-Sb-O activated GaAs photocathodes at 200 keV with 1 mA average beam current to observe if a more chemically robust activation layer translated into an improvement in the charge lifetime under a high voltage environment. We observed a 45% improvement in charge lifetime at 780 nm for the Cs-Sb-O activated GaAs. This improvement at infrared wavelength does not correspond to an improvement at 488 nm, where instead, the lifetime was shorter. These results are interpreted in terms of work function increase induced by ion-back-bombardment. The larger lifetime at 780 nm suggests a smaller work function increase for the Cs-Sb-O case. Our results show that lifetime measurements at a single wavelength are not sufficient to fully characterize the robustness of NEA layers in operational conditions.

For future works, characterizing spectral response during the beam operation can help understand the nature of spectral dependence of lifetime improvements. The effect of thermal desorption also needs to be identified. Lastly, Cs-Sb-O activated GaAs can have a high initial QE by activating in a chamber connected to the beamline.

4.7 Acknowledgments

This work was supported by the Department of Energy under Grant No.DE-SC0021425 and the National Science Foundation under Grant No.PHY-1549132, the Center for Bright Beams. The authors would like to acknowledge Joe Grames for valuable discussions.

5

Brightness of femtosecond nonequilibrium photoemission in metallic photocathodes at wavelengths near the photoemission threshold

This chapter was originally published as Ref. [19].

5.1 Abstract

The operation of photoemission electron sources with wavelengths near the photoemission threshold has been shown to dramatically decrease the minimum achievable photocathode emittance, but at the cost of significantly reduced quantum efficiency (QE). In this work, we show that for femtosecond laser and electron pulses, the increase in required laser intensities due to the low QE drives the photocathode electronic distribution far from static equilibrium. We adapt an existing dynamic model of the electron occupation under high intensity laser illumination to predict the time-dependent effects of the nonequilibrium electron distribution on the QE, mean transverse energy (MTE), and

emission brightness of metal phtocathodes. We find that multiphoton photoemission dramatically alters the MTE as compared to thermal equilibrium models, causing the MTE to no longer be a monotonic function of photon excess energy.

5.2 Introduction

Ultrafast electron pulses generated from photocathode sources play a critical role in probing time-resolved ultrafast dynamics, in applications ranging from free electron lasers [118] to ultrafast electron diffraction [119] and microscopy [120]. For each of these cases, the critical figure of merit is the 5D beam brightness. In a linear accelerator, the beam brightness is never larger than it is at the photoemission source, and is thus given by [121, 23, 10]:

$$\mathcal{B}_{5D,max} \equiv \frac{1}{16\pi^2}\frac{I}{\epsilon_x\epsilon_y} = \frac{1}{16\pi^2}\frac{Im_ec^2}{\sigma_x\sigma_y\mathrm{MTE}} \tag{5.1}$$

where I is the peak current from the cathode, $\epsilon_{x,y}$ is the normalized emittance of the beam, $\sigma_{x,y}$ is the rms laser spot size, m_ec^2 is the electron rest energy, and MTE is the mean transverse energy of the photoelectrons at the photocathode [18]. The laser spot size is primarily determined by the space charge beam dynamics after photoemission. The MTE is determined by material properties that affect the photoemission process inside the photocathode, the cathode surface, and the photoemission drive laser properties.

Dowell and Schmerge demonstrated that Spicer's three-step photoemission model [20] can be utilized to derive expressions for the photoemission quantum efficiency (QE) and MTE of metal photocathodes [7]. While this was originally derived under the assumption of a free electron Fermi gas and a flat density

of states at zero temperature, recent studies have extended this approach to account for a realistic density of states and non-zero (but constant) electronic temperature (T_e) [9, 8]. These models predict that as the photon energy ($h\nu$) approaches the work function (ϕ), MTE converges to the thermal energy of electrons (MTE $\approx k_B T_e$). For a photon energy well above the threshold ($h\nu - \phi \gg 0$), the MTE is linear in the photon excess energy, MTE $\approx (h\nu - \phi)/3$. Both behaviors have been demonstrated experimentally [8]. These studies predict that MTE is minimized by operating with very low photon excess energy, but do not account for dynamic or intensity dependent effects, such as multiphoton excitation or laser-induced ultrafast electron heating.

Metallic photocathodes, and in particularly copper photocathodes, are popular choices for ultrafast electron sources due to their prompt response time (< 50 fs) and moderate vacuum requirements [23, 24]. However, compared to semiconducting emitters, they suffer from several orders of magnitude less QE, due to frequent electron-electron scattering during the transport of the excited population from the bulk to the surface. Thus, metallic photocathodes can demand a very high laser intensity (10s of $\mathrm{GW/cm^2}$) for femtosecond emission cases, for example in the blowout regime [25] of high charge photoinjectors.

It has long been known that under high fluence, short pulse laser irradiation, the electronic temperature of the illuminated material can reach several thousand Kelvin for several picoseconds, while the lattice remains relatively cold [122, 123, 124]. It was recently pointed out that this effect can drive up the minimum achievable photoemission MTE, and was calculated by using the traditional two temperature model coupled with the extended Dowell-Schmerge photoemission relations [23]. Two temperature models naturally assume the

underlying electronic distribution remains approximately thermalized, which may not be the case for femtosecond duration illumination. Furthermore, there have been experimental efforts which highlight the importance of multiphoton and heating effects on intense femtosecond photoemission [125, 126, 127].

Femtosecond dynamics of photoexcited electrons in copper has been studied experimentally by time-resolved photoemission spectroscopy [128, 129, 130]. For theoretical understanding and predictions, Rethfeld *et al.* suggested using the Boltzmann equation for nonequilibrium thermodynamics of metals irradiated by high laser fluence [131, 132, 133]. It was shown that this approach also allows simulating dynamic effects of photoemission, such as the image-charge driven reduction of the work function via a time dependent space charge field [11]. In this paper, we extend the Rethfeld approach to calculate key brightness parameters (QE and MTE) of a photocathode under high fluence ($\sim$ 1 mJ/cm^2) laser irradiation for femtosecond electron pulse applications. The model has the capability to account for femtosecond nonequilibrium thermodynamics, multiphoton absorption, and a realistic density of states.

5.3 Boltzmann equation

Before photons arrive at the cathode, the initial electronic occupation function, $f(\vec{k})$, is in thermal equilibrium, and thus follows the Fermi-Dirac distribution. As photons begin to interact with electrons, the electronic occupation changes as a function of time, and we can calculate this change for each time step according to the Boltzmann equation:

$$\frac{df(\vec{k},t)}{dt} = \left.\frac{\partial f(\vec{k},t)}{\partial t}\right|_{el-el} + \left.\frac{\partial f(\vec{k},t)}{\partial t}\right|_{photon\ absorb} \tag{5.2}$$

where the first and second terms represent the occupation function change due to electron-electron collisions and photon absorption respectively. Here and throughout we have neglected the effects of electron-phonon interactions due to the very short timescale ($\leq$ 100 fs) of the laser pulses considered. Furthermore, thermal conductivity and all spatial variation of the laser intensity is ignored, which is valid only for the case of homogeneous thin film photocathodes [132].

Whereas the photon absorption term in Eq. 5.2 drives the distribution away from thermal equilibrium, the electron-electron scattering term regulates the thermalization timescale. As in Ref. [132], the electron-electron scattering term is calculated based on the Coulomb interaction of two electrons that obey energy conservation ($\Delta E = E_2 - E_1 = E_3 - E$) and momentum conservation ($\Delta\vec{k} = \vec{k_2} - \vec{k_1} = \vec{k_3} - \vec{k}$).[131, 132] Here, $\vec{k}, \vec{k_2}$ are initial wave vectors, and $\vec{k_1}, \vec{k_3}$ are final wave vectors of the two interacting electrons. Assuming an isotropic system, the Fourier transform of the screened Coulomb potential $V_{ee}(r) = \frac{e^2}{4\pi\epsilon_0}\frac{1}{r}e^{-\kappa r}$ yields [134, 131]:

$$|M_{ee}(\Delta k, \kappa)|^2 = \Big(\frac{e^2}{\epsilon_0 \Omega}\frac{1}{|\Delta k|^2 + \kappa^2}\Big)^2 \tag{5.3}$$

where Ω is the unit cell volume, and

$$\kappa^2(t) = \frac{e^2}{\epsilon_0}\int_0^\infty dE D(E)\frac{df(E,t)}{dE} \tag{5.4}$$

is the screening parameter with $D(E)$ as the density of state per volume for copper.[135] The density of states is assumed to be flat for energy 6 eV above the Fermi level. Then, due to Fermi's golden rule, the change in the occupation due to electron-electron collision processes is given by [132, 131]:

$$\frac{\partial f(\vec{k})}{\partial t}\Big|_{el-el} = \frac{2\pi}{\hbar}\sum_{\vec{k_1}}\sum_{\vec{k_3}}|M_{ee}|^2 \mathcal{F}\,\delta(E_i - E_f). \tag{5.5}$$

Here, $\delta(E_i - E_f)$ ensures the energy conservation between the initial ($E_i = E + E_2$) and final energy ($E_f = E_1 + E_3$), and $\mathcal{F}$ is the Pauli exclusion principle term

expressed with occupation functions, $f_i \equiv f(k_i)$ [131, 132, 133]:

$$\mathcal{F} = f_1 f_3 (1 - f)(1 - f_2) - f f_2 (1 - f_1)(1 - f_3). \tag{5.6}$$

In this work, we further assume the system to be described by an isotropic single band model, which in analogy with the free electron case yields:

$$|k(E)|^3 = 3\pi^2 \int_0^E d\epsilon D(\epsilon). \tag{5.7}$$

Consequently, Eq. 5.5 can be further simplified as in Ref. [132].

The effective one band assumption requires a mediating body to conserve momentum upon photon absorption. Here the inverse bremsstrahlung model is used: quasifree electrons absorb photons mediated by Coulomb potential from an ion [136, 131]. Here, the electron mass is negligible compared to the ion mass. Therefore, the momentum conservation holds for an arbitrary final momentum ($\vec{k} + \Delta\vec{k} = \vec{k_f}$) while there is no energy transfer to the ion ($E = E_f$). The Coulomb interaction between an electron and ion has mathematically identical expression to Eq. 5.3. Additionally, the interaction between the electron and photon introduces a Bessel function term, $J_\ell^2(e\vec{E_L} \cdot \Delta\vec{k}/m_e\omega_L^2)$, multiplied to the Coulomb potential term where ℓ is the number of photons absorbed, ω_L is the angular frequency of the laser light, and $\vec{E_L}$ is the electric field from the photons [137]. Hence, the Fermi's golden rule is given by:

$$\left.\frac{\partial f(\vec{k})}{\partial t}\right|_{photon\ absorb} = \frac{2\pi}{\hbar} \sum_{\Delta\vec{k}} \sum_{\ell} |M_{ee}|^2 J_\ell^2 \mathcal{F} \delta(E - E_f) \tag{5.8}$$

where $\mathcal{F}$ is again the Pauli exclusion principle term [131, 132]:

$$\mathcal{F} = f(k_f)(1 - f(k)) - f(k)(1 - f(k_f)). \tag{5.9}$$

Analogous to Eq. 5.5, the simplified expression of Eq. 5.8 from Ref. [132] is used throughout in our work. It is important to note that this model allows for both

the simultaneous (via the power series in ℓ) and subsequent (time delayed) absorption/emission of multiple photons. However, the simultaneous (or coherent) multiphoton absorptions are suppressed in this model due to single band assumption.

Based on Eq. 5.2, 5.5, and 5.8, one can calculate the electronic distribution $f(E,t)$ as a function of energy and time. To investigate the dynamics of electron energy distribution of copper during and after 50 fs laser irradiation, we perform a quasilogarithmic transformation of the occupation function $f(E,t)$ as proposed in Ref. [133]:

$$\Phi[f(E,t)] \equiv -\ln[1/f(E,t) - 1]. \tag{5.10}$$

Under this transformation, a Fermi-Dirac distribution has a linear relation with energy where its slope is inversely proportional to the temperature. Note that nonlinearity in energy indicates nonequilibrium behavior. In Fig. 5.1, a quasilogarithmic transformation of the occupation functions of copper under 50 fs laser irradiation is plotted for two different absorbed fluences at four different time positions (0 fs, 10 fs, 50 fs, and 100 fs from the beginning of the laser irradiation). The initial distribution demonstrates a perfect linear relation in thermal equilibrium of 300 K whereas the occupation functions during the laser irradiation ($0 < t \leq 50$ fs) show strong nonlinearity due to nonequilibrium dynamics. At 100 fs, the high fluence irradiated electrons approach another thermal equilibrium of ~3500 K while the low fluence irradiated electrons are still far from thermalization. It was reported that a smaller fluence irradiation tends to have a longer thermalization timescale up to several hundred femtoseconds [132].

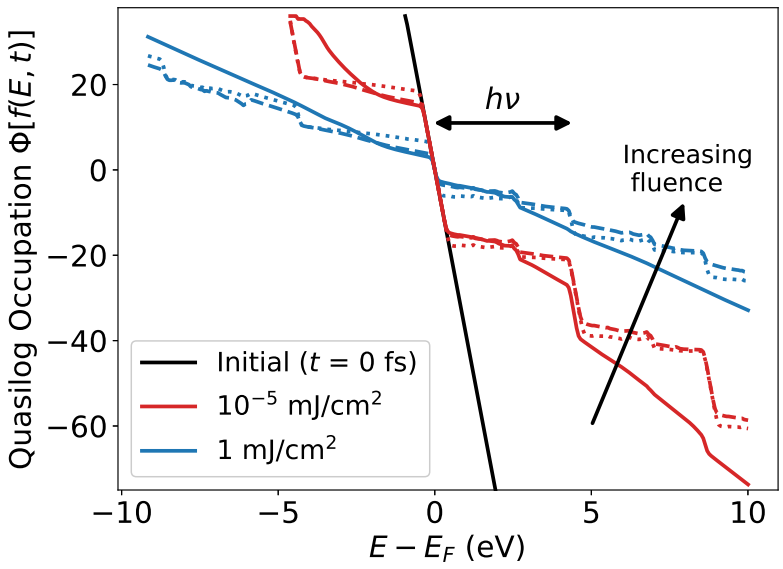

Figure 5.1: Quasilogarithmic transformation of electron energy distribution $\Phi[f(E,t)]$ of copper over time (Eq. 5.10). Under 50 fs laser irradiation, the work function photon energy of 4.31 eV was used with two different laser intensities that results in 1 mJ/cm^2 (blue) and 10^{-5} mJ/cm^2 (red) absorbed fluences. The transient distributions are plotted at t = 0 fs (black solid line), 10 fs (dotted lines), 50 fs (dashed lines), and 100 fs (colored solid lines).

5.4 Calculation of QE and MTE in nonequilibrium conditions

The QE and MTE can be simulated by determining the number and energy distribution of electrons promoted above the vacuum level based on numerically calculated time dependent occupation function $f(E,t)$ from the previous section. The energy distribution of electrons above the vacuum level parameters is dynamic, meaning that the efficiency, MTE, and photoemitted pulse shape are nontrivial functions of time.

QE is defined as the number of electrons emitted by the photocathode divided by the number of photons incident on the photocathode surface. To cal-

culate the number of emitted electrons, we express the partial current density of electrons per energy E in the direction θ away from the normal direction as:

$$j(E,t,\theta) \equiv e f(E,t) D(E) v(E) \cos\theta \tag{5.11}$$

where e is the electron charge, and $v(E)$ is the speed of electrons ($\hbar k(E)/m_e$). Then, the total number of escaped electrons per unit area can be derived by integrating this flux over time (t), energy above the vacuum level ($E > E_F + \phi$), and allowed directions of the escape velocity ($\cos\theta > \cos\theta_E \equiv \sqrt{(E_F+\phi)/E}$):[7]

$$N_e = \frac{\displaystyle\int_0^t dt' \int_{E_F+\phi}^{\infty} dE \int_{\cos\theta_E}^{1} d(\cos\theta) \frac{j(E,t',\theta)}{e}}{\displaystyle\int_{-1}^{1} d(\cos\theta)}. \tag{5.12}$$

Although it may be intuitive to calculate the number of photons in each pulse based on the input parameters from Eq. 5.8, it was shown that inverse bremsstrahlung process, which accounts only intraband absorption, does not produce the correct optical skin depth of the material [133]. The discrepancy can be up to a factor of 2 for the range of photon energy used in our work. Therefore, instead of using the input parameters, the number of absorbed photons is calculated *post-facto* based on the change of internal energy for unit volume, ΔE:

$$N_{ph} = \frac{d_s \Delta E}{\hbar\omega_L} = \frac{d_s}{\hbar\omega_L} \int_0^{\infty} dE\, D(E)[f(E,t) - f(E,0)]E. \tag{5.13}$$

Here, the optical skin depth, d_s = 13 nm,[138] is multiplied to calculate the number of absorbed photons for unit area. Finally, the QE is expressed as:

$$\text{QE} = N_e(1-R)/N_{ph} \tag{5.14}$$

where R is the reflectivity of copper [138].

MTE is the averaged transverse energy ($(p \sin\theta)^2/2m_e$) of electrons above the vacuum level. As in the Dowell-Schmerge model, we assume no effects of the electron effective mass on the MTE, and thus set $p^2/2m_e = E$. Similar to Eq. 5.12, we get MTE by integrating over time, energy, and allowed angle:

$$\mathrm{MTE} = \frac{\int_0^t dt' \int_{E_F+\phi}^{\infty} dE \int_{\cos\theta_E}^{1} d(\cos\theta)\, j(E,t',\theta) E \sin^2\theta}{\int_0^t dt' \int_{E_F+\phi}^{\infty} dE \int_{\cos\theta_E}^{1} d(\cos\theta)\, j(E,t',\theta)}. \tag{5.15}$$

Due to discretization of the energy distribution, the uncertainty of calculated MTE is ~ 5 meV.

5.5 Results: QE and MTE

We first set the absorbed laser fluence down to single-photon absorption dominant regime (10^{-5} mJ/cm^2) to compare with experimentally measured QE [6] and earlier predictions on MTE [7, 8, 9]. For a pulse length of 50 fs, the QE and MTE for a copper photocathode with a realistic density of states are plotted in Fig. 5.2 based on Eq. 5.14 and Eq. 5.15. Throughout the calculations, 4.31 eV was used for the work function (ϕ) [6]. The quantum efficiency demonstrates very good agreement with experimentally measured values from a copper photocathode cleaned by a hydrogen ion beam in situ [6]. Furthermore, the asymptotic properties of MTE is consistent with earlier predictions [7, 8, 9].

A generalized Fowler-DuBridge analysis [139, 140] was performed to investiagte the contribution of multiphoton effects in the QE and MTE. Bechtel extended Fowler-DuBridge theory for multiphoton photoemission suggests that

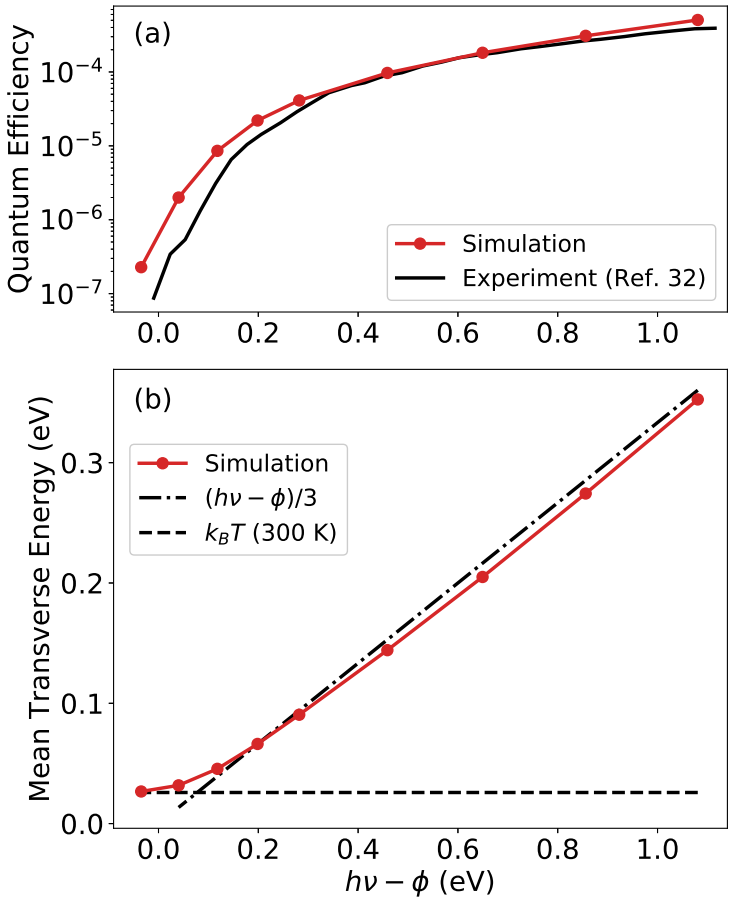

Figure 5.2: (a) QE calculated based on Eq. 5.14 in single photon absorption dominant regime (10^{-5} mJ/cm^2 absorbed fluence), compared to experimentally measured values [6]. (b) MTE computed by Eq. 5.15 as a function of excess photon energy ($h\nu - \phi$) for 10^{-5} mJ/cm^2 absorbed fluence. The dashed line represents the thermal energy. The dash-dotted line is a linear relation predicted and confirmed in earlier works [7, 8, 9].

the total photocurrent density J can be expressed as a sum of partial current densities due to n-photon absorption J_n [141, 142, 143]:

$$J = \sum_{n=0}^{\infty} J_n = \sum_{n=0}^{\infty} \sigma_n I^n \tag{5.16}$$

where J_n is proportional to the n-th power of the intensity of incident laser I, and σ_n is the series coefficient. Hence, the fraction of singly excited electrons

among all emitted electrons can be calculated as [126]:

$$\frac{J_1}{J} = \frac{\sigma_1 I}{\sum_{n=0}^{\infty} \sigma_n I^n}. \tag{5.17}$$

In Fig. 5.3, the total number of emitted electrons N_e (Eq. 5.12) is fitted to a fourth degree polynomial function of absorbed fluence (Eq. 5.13), to plot the fraction of singly excited electrons above the vacuum level. For the 10^{-5} mJ/cm^2 absorbed fluence used in Fig. 5.2, single photon absorbed electrons dominate the emission spectrum for all photon energies greater than the work function (See Fig. 5.3 (b)). Thus, the calculated photoemission parameters are essentially determined by singly excited electrons and agree well with conventional, static models that only consider single photon absorption. However, as the absorbed fluence increases, the fraction of electrons that absorbs a single photon drops rapidly near the threshold ($h\nu - \phi \approx 0$), and multiphoton absorbed electrons are no longer negligible in calculation of QE and MTE.

To demonstrate the effect of using high fluence laser, QE and MTE are re-calculated in Fig. 5.4 with 1 mJ/cm^2 absorbed fluence. For photon energies well above the threshold, it is noteworthy that both QE and MTE values are near those in the low fluence simulation. This is consistent with Fig. 5.3, as singly excited electrons account for the majority of electrons that have escaped even at high fluence with high photon excess energy. On the other hand, as the photon energy approaches to the work function ($h\nu - \phi \approx 0$), the fraction of singly-excited emitted electrons rapidly decreases (See Fig. 5.3(b)). This tendency is also enhanced by the fact that the allowed direction of the escape velocity ($\cos\theta > \sqrt{(E_F + \phi)/E}$) is substantially suppressed near the threshold energy ($E_F + \phi$) of electrons. Hence, doubly excited electrons occupy non-negligible portion of the total emitted charge for photon energies that are 100s of meV above the work function, and they yield a non-monotonic behavior of MTE as a func-

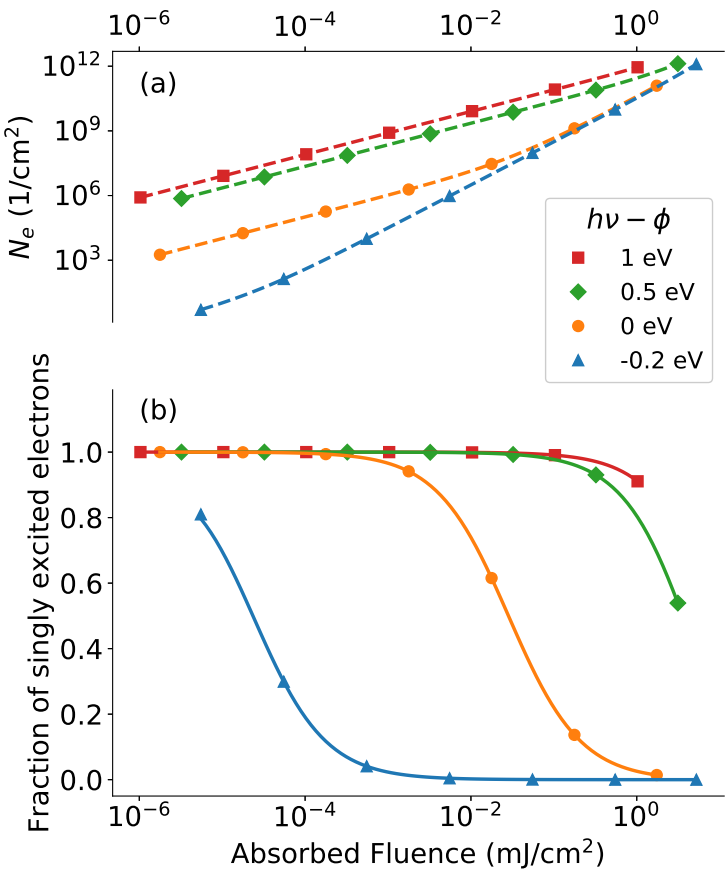

Figure 5.3: (a) The total number of extracted electrons in each pulse for unit area fitted to a fourth degree polynomial function of absorbed fluence. (b) Fraction of singly excited electrons calculated based on generalized Fowler-DuBridge theory using Eq. 5.17.

tion of the photon excess energy ($h\nu - \phi$) in Fig. 5.4. If the photon energy falls below the work function, single photon absorption can no longer contribute electrons above the vacuum level, so the photoemission parameters are essentially dominated by two-photon absorption alone. Thus, once photoemission is entirely dominated by two photon effects, a further reduction of the photon excess energy once again yields a reduction of the MTE, but the thermal value is never achieved.

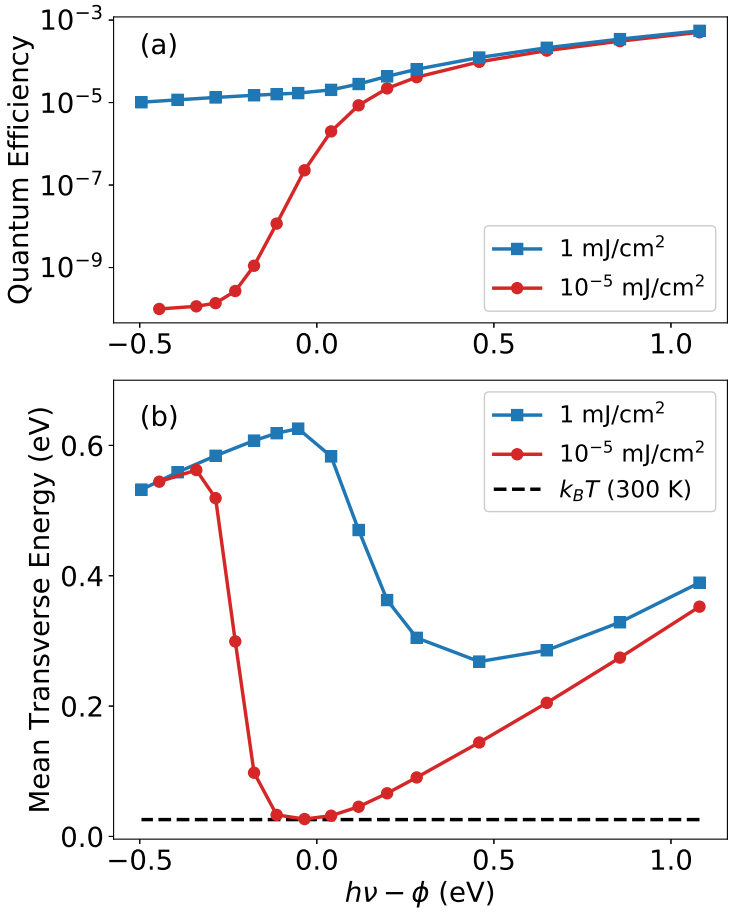

Figure 5.4: (a) QE computed by Eq. 5.14 for a high fluence of 1 mJ/cm^2, compared to the low fluence (10^{-5} mJ/cm^2) simulation over extended photon energy range. (b) MTE calculated based on Eq. 5.15 for 1 mJ/cm^2 and 10^{-5} mJ/cm^2 absorbed fluences. Two-photon absorbed electrons cause the non-monotonic behavior of MTE.

Recently, increase of intrinsic emittance induced by multiphoton photoemission from copper photocathodes under femtosecond laser illumination was experimentally verified [126], and showed qualitative agreement with our results. In that work, the growth of MTE was observed at the absorbed fluence of 7×10^{-6} mJ/cm^2 with the photon energy 0.2 eV below the effective work function. According to our simulation in Fig. 5.3, the fraction of singly excited electrons is $\sim$ 76% for a similar laser profile. When the photon energy range was

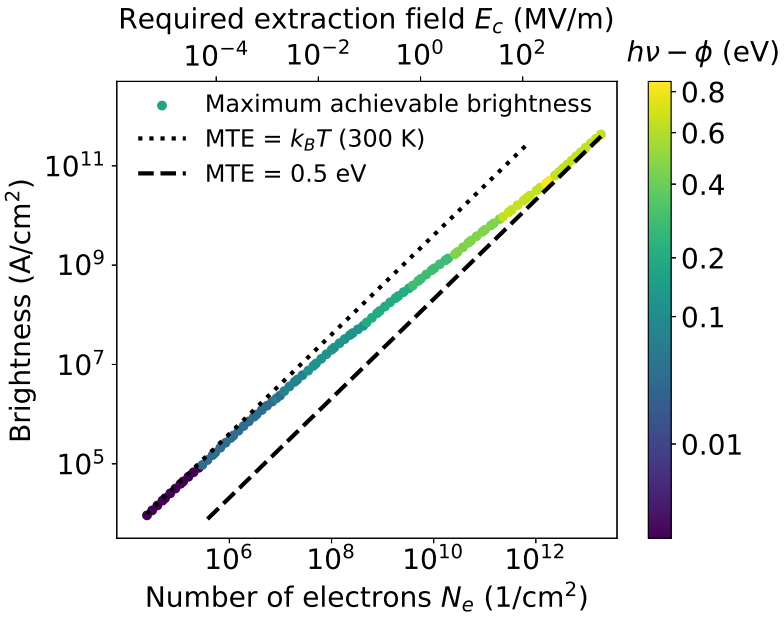

Figure 5.5: Maximum achievable brightness calculated by Eq. 5.1 as a function of the number of extracted electrons from Eq. 5.12 and the required extraction electric field under the pancake aspect ratio approximation [10, 11]. The color scale represent the input photon energy to obtain the corresponding maximum achievable brightness. The dotted line and dashed line illustrate brightness calculated using fixed MTE. One thousand sets of photon energy and laser fluence were simulated to acquire maximum achievable brightness.

extended below the threshold for the low fluence simulation in Fig. 5.4, we also observe the MTE growth. Note the non-monotonic behavior of MTE can be captured theoretically only when multiphoton absorption is considered.

5.6 Brightness

One of notable aspects of the high fluence laser irradiation simulation in Fig. 5.4 is that the laser photon energy can be tuned to minimize MTE, thereby maximizing brightness for a fixed laser fluence. Therefore, by iterating over numerous

input laser fluences and photon energies, one can plot the maximum achievable brightness for a given number of extracted electrons per pulse and the corresponding required extraction field E_c as in Fig. 5.5. In the pancake aspect ratio regime, the charge density is directly proportional to the required extraction electric field, $eN_e = \epsilon_0 E_c$ [10, 11]. Here, the brightness and the number of electrons for a 50 fs flat top pulse are calculated by Eq. 5.1 and Eq. 5.12, respectively. The color scale shows the optimal photon energy above the threshold used to obtain the maximum brightness for corresponding charge extraction per pulse. Two features are of note. First, the optimal photon energy can be well above the threshold depending on desired amount of charge extraction for specific applications. Second, the maximum brightness as a function of the extracted areal charge density is no longer linear, but rather at 100 MV/m equivalent space charge fields the maximum brightness is reduced below the room temperature limit by a factor of ~ 12.

5.7 Conclusion

We have presented photoemission simulations using a Boltzmann equation method that has capability to account nonequilibrium thermodynamics and multiphoton photoemission. Using a low absorbed fluence (10^{-5} mJ/cm^2), the calculated photoemission parameters reproduced the experimentally measured QE and demonstrated good agreement of MTE with earlier, static equilibrium predictions due to the abundance of singly excited electrons. In contrast, for a high absorbed fluence (1 mJ/cm^2), multiphoton absorbed electrons are no longer negligible especially near the threshold photon energy, thereby causing the growth of MTE. Since the minimum MTE is no longer the thermal energy

and not achieved by the work function photon energy, a series of laser fluences were simulated to plot the maximum achievable brightness for a given number of extracted electrons in a 50 fs pulse. Our results illustrate the importance of multiphoton effects on beam brightness of photocathodes for femtosecond applications. A dynamic photoemission calculation like the one presented here could be self-consistently coupled to a space charge dynamics tracking code for precision photoinjector modeling.

5.8 Acknowledgments

This work was supported by the U.S. National Science Foundation under award PHY-1549132, the Center for Bright Beams.

6 Conclusion

An electron source capable of sustaining high-intensity production of spin-polarized electrons is highly sought after for both current and future nuclear and high energy physics facilities, such as the Electron Ion Collider and the International Linear Collider [13, 144, 14]. Furthermore, electron microscopy techniques can utilize spin-polarized electrons to study magnetization in materials and nanostructures [86, 17, 87]. A Negative Electron Affinity (NEA) activated GaAs in a high voltage electron gun is the best option to date to produce a highly spin-polarized electron beam at a high current. However, extreme vaccum sensitivity of NEA layer is the main drawback that results in rapid Quantum Efficiency (QE) degradation over time; hence it has a short operational lifetime [4, 55, 66, 5]. Traditional NEA activation layers such as Cs-O_2 and Cs-NF_3 form a monolayer that is chemically reactive and weakly bound to the surface [57, 56]. Recent studies showed that robust solar-blind material Cs_2Te could also form NEA on GaAs due to a peculiar alignment of the electronic bands [2, 64, 65].

In this thesis, we first activated GaAs with Cs_2Te to characterize various photocathode parameters. We obtained a similar spectral response to Ref. [2] and confirmed NEA activation on GaAs. Auger electron spectroscopy was used to

study the NEA surface elements. QE at 532 nm was monitored while extracting current to characterize the lifetime. We achieved a factor of 5 improvements in the lifetime at 532 nm compared to the standard Cs-O activated GaAs. A Mott polarimeter was used to characterize the degree of spin polarization. Despite a thicker NEA layer of Cs_2Te, the spin polarization was not affected.

Based on the heterojunction model between GaAs and Cs_3Sb, we were motivated to study activation of GaAs using Cs_3Sb. It was discovered that codepositing oxygen during the growth can increase the QE at 780 nm without a significant decrease in the photocathode lifetime. We obtained one order of magnitude improvement in a lifetime at 505 nm and a factor of 7 improvements in a lifetime at 780 nm. Similar to the previous study, spin polarization was minimally affected. Furthermore, a superlattice sample was activated with Cs-Sb-O and compared to the standard activated sample. 90% spin polarization was preserved with a factor of 7 improvements in a lifetime at 780 nm.

Although lifetime improvements were demonstrated in the previous works, these photoemission measurements were done with a 10's of eV bias and 100's of nA beam current, which is significantly different from the harsh environment of an electron gun that operates on the scale of 100's of keV. Specifically, the amount of current extracted and the energy-dependent residual gas ionization cross-sections are orders of magnitude different [4]. Furthermore, the primary QE degradation mechanism was chemical poisoning in our previous works as opposed to ion back bombardment [5]. We recommissioned a high voltage DC gun and operated Cs-Sb-O and Cs-O activated GaAs photocathodes in order to make a direct comparison of their performance at 200 keV beam energy at 1 mA average current –the ultimate test required to establish the photocathode

performance under "real life" conditions. We observed spectral dependence on the lifetime improvement. In particular, we saw a 45% increase in the lifetime at 780 nm for Cs-Sb-O activated GaAs compared to Cs-O activated GaAs.

Chapter 5 presents photoemission simulations of Cu photocathode using a Boltzmann equation method that has capability to account nonequilibrium thermodynamics and multiphoton photoemission. Using a low absorbed fluence (10^{-5} mJ/cm^2), the calculated photoemission parameters reproduced the experimentally measured QE and demonstrated good agreement of MTE with earlier, static equilibrium predictions due to the abundance of singly excited electrons. In contrast, for a high absorbed fluence (1 mJ/cm^2), multiphoton absorbed electrons are no longer negligible especially near the threshold photon energy, thereby causing the growth of MTE. Since the minimum MTE is no longer the thermal energy and not achieved by the work function photon energy, a series of laser fluences were simulated to plot the maximum achievable brightness for a given number of extracted electrons in a 50 fs pulse. Our results illustrate the importance of multiphoton effects on beam brightness of photocathodes irradiated by high intensity laser. This work implies that such multiphoton effects are significant for other photocathodes as well for femtosecond applications, including GaAs-based photocathodes.

Bibliography

[1] Wei Liu, Matt Poelker, Xincun Peng, Shukui Zhang, and Marcy Stutzman. A comprehensive evaluation of factors that influence the spin polarization of electrons emitted from bulk GaAs photocathodes. *Journal of Applied Physics*, 122(3):035703, July 2017.

[2] Masao Kuriki, Yuji Seimiya, Kazuhide Uchida, and Kashiwagi Shigeru. GaAs Photocathode Activation with CsTe Thin Film. *Proceedings of IPAC2015*, 2015.

[3] G. Vergara, A. Herrera-Gómez, and W. E. Spicer. Calculated electron energy distribution of negative electron affinity cathodes. *Surface Science*, 436(1):83–90, 1999.

[4] J. Grames, R. Suleiman, P. A. Adderley, J. Clark, J. Hansknecht, D. Machie, M. Poelker, and M. L. Stutzman. Charge and fluence lifetime measurements of a dc high voltage GaAs photogun at high average current. *Physical Review Special Topics - Accelerators and Beams*, 14(4):043501, April 2011.

[5] Luca Cultrera, Alice Galdi, Jai Kwan Bae, Frank Ikponmwen, Jared Maxson, and Ivan Bazarov. Long lifetime polarized electron beam production from negative electron affinity GaAs activated with Sb-Cs-O: Trade-offs between efficiency, spin polarization, and lifetime. *Physical Review Accelerators and Beams*, 23(2):023401, February 2020.

[6] D. H. Dowell, F. K. King, R. E. Kirby, J. F. Schmerge, and J. M. Smedley.

In situ cleaning of metal cathodes using a hydrogen ion beam. *Phys. Rev. Spec. Top. - Accel. Beams*, 9(6):1–8, 2006.

[7] David H. Dowell and John F. Schmerge. Quantum efficiency and thermal emittance of metal photocathodes. *Physical Review Special Topics - Accelerators and Beams*, 12(7):074201, July 2009.

[8] Jun Feng, J. Nasiatka, Weishi Wan, Siddharth Karkare, John Smedley, and Howard A. Padmore. Thermal limit to the intrinsic emittance from metal photocathodes. *Appl. Phys. Lett.*, 107(13), 2015.

[9] D. A. Dimitrov, G. I. Bell, J. Smedley, I. Ben-Zvi, J. Feng, S. Karkare, and H. A. Padmore. Modeling quantum yield, emittance, and surface roughness effects from metallic photocathodes. *J. Appl. Phys.*, 122(16), 2017.

[10] Ivan V. Bazarov, Bruce M. Dunham, and Charles K. Sinclair. Maximum achievable beam brightness from photoinjectors. *Phys. Rev. Lett.*, 102(10):2–5, 2009.

[11] W. Wendelen, B. Y. Mueller, D. Autrique, A. Bogaerts, and B. Rethfeld. Modeling ultrashort laser-induced emission from a negatively biased metal. *Appl. Phys. Lett.*, 103(22), 2013.

[12] P Musumeci, J Giner Navarro, JB Rosenzweig, L Cultrera, I Bazarov, J Maxson, S Karkare, and H Padmore. Advances in bright electron sources. *Nuclear Instruments and Methods in Physics Research Section A: Accelerators, Spectrometers, Detectors and Associated Equipment*, 907:209–220, 2018.

[13] Erdong Wang, Omer Rahman, John Skaritka, Wei Liu, Jyoti Biswas, Christopher Degen, Patrick Inacker, Robert Lambiase, and Matthew Paniccia. High voltage dc gun for high intensity polarized electron source. *Physical Review Accelerators and Beams*, 25(3):033401, 2022.

[14] Hiroaki Aihara, Jonathan Bagger, Philip Bambade, Barry Barish, Ties Behnke, Alain Bellerive, Mikael Berggren, James Brau, Martin Breidenbach, Ivanka Bozovic-Jelisavcic, Philip Burrows, Massimo Caccia, Paul Colas, Dmitri Denisov, Gerald Eigen, Lyn Evans, Angeles Faus-Golfe, Brian Foster, Keisuke Fujii, Juan Fuster, Frank Gaede, Jie Gao, Paul Grannis, Christophe Grojean, Andrew Hutton, Marek Idzik, Andrea Jeremie, Kiyotomo Kawagoe, Sachio Komamiya, Tadeusz Lesiak, Aharon Levy, Benno List, Jenny List, Shinichiro Michizono, Akiya Miyamoto, Joachim

Mnich, Hugh Montgomery, Hitoshi Murayama, Olivier Napoly, Yasuhiro Okada, Carlo Pagani, Michael Peskin, Roman Poeschl, Francois Richard, Aidan Robson, Thomas Schoerner-Sadenius, Marcel Stanitzki, Steinar Stapnes, Jan Strube, Atsuto Suzuki, Junping Tian, Maksym Titovx, Marcel Vos, Nicholas Walkerx, Hans Weise, Andrew White, Graham Wilson, Marc Winter, Sakue Yamada, Akira Yamamoto, Hitoshi Yamamoto, and Satoru Yamashita. The International Linear Collider. A Global Project. *arXiv:1901.09829 [hep-ex, physics:physics]*, January 2019.

[15] W al Ackermann, G Asova, V Ayvazyan, A Azima, N Baboi, J Bähr, V Balandin, B Beutner, A Brandt, A Bolzmann, et al. Operation of a free-electron laser from the extreme ultraviolet to the water window. *Nature photonics*, 1(6):336–342, 2007.

[16] DA Orlov, U Weigel, D Schwalm, AS Terekhov, and A Wolf. Ultra-cold electron source with a gaas-photocathode. *Nuclear Instruments and Methods in Physics Research Section A: Accelerators, Spectrometers, Detectors and Associated Equipment*, 532(1-2):418–421, 2004.

[17] M. Kuwahara, S. Kusunoki, X. G. Jin, T. Nakanishi, Y. Takeda, K. Saitoh, T. Ujihara, H. Asano, and N. Tanaka. 30-kV spin-polarized transmission electron microscope with GaAs–GaAsP strained superlattice photocathode. *Applied Physics Letters*, 101(3):033102, July 2012.

[18] P. Musumeci, J. Giner Navarro, J. B. Rosenzweig, L. Cultrera, I. Bazarov, J. Maxson, S. Karkare, and H. Padmore. Advances in bright electron sources. *Nucl. Instruments Methods Phys. Res. Sect. A Accel. Spectrometers, Detect. Assoc. Equip.*, 2018.

[19] Jai Kwan Bae, Ivan Bazarov, Pietro Musumeci, Siddharth Karkare, Howard Padmore, and Jared Maxson. Brightness of femtosecond nonequilibrium photoemission in metallic photocathodes at wavelengths near the photoemission threshold. *Journal of Applied Physics*, 124(24):244903, December 2018.

[20] C. N. Berglund and W. E. Spicer. Photoemission studies of copper and silver: Theory. *Phys. Rev.*, 136(4A), 1964.

[21] Conyers Herring and MH Nichols. Thermionic emission. *Reviews of modern physics*, 21(2):185, 1949.

[22] Philip E Batson, Niklas Dellby, and Ondrej L Krivanek. Sub-ngstrom res-

olution using aberration corrected electron optics. *Nature*, 418(6898):617–620, 2002.

[23] J. Maxson, P. Musumeci, L. Cultrera, S. Karkare, and H. Padmore. Ultrafast laser pulse heating of metallic photocathodes and its contribution to intrinsic emittance. *Nucl. Instruments Methods Phys. Res. Sect. A Accel. Spectrometers, Detect. Assoc. Equip.*, 865:99–104, 2017.

[24] R. K. Li, H. To, G. Andonian, J. Feng, A. Polyakov, C. M. Scoby, K. Thompson, W. Wan, H. A. Padmore, and P. Musumeci. Surface-plasmon resonance-enhanced multiphoton emission of high-brightness electron beams from a nanostructured copper cathode. *Phys. Rev. Lett.*, 110(7):1–5, 2013.

[25] P. Musumeci, J. T. Moody, R. J. England, J. B. Rosenzweig, and T. Tran. Experimental generation and characterization of uniformly filled ellipsoidal electron-beam distributions. *Phys. Rev. Lett.*, 100(24):1–4, 2008.

[26] Evan R Antoniuk, Peter Schindler, W Andreas Schroeder, Bruce Dunham, Piero Pianetta, Theodore Vecchione, and Evan J Reed. Novel ultrabright and air-stable photocathodes discovered from machine learning and density functional theory driven screening. *Advanced Materials*, 33(44):2104081, 2021.

[27] Károly Németh, Katherine C Harkay, Michel van Veenendaal, Linda Spentzouris, Marion White, Klaus Attenkofer, and George Srajer. High-brightness photocathodes through ultrathin surface layers on metals. *Physical review letters*, 104(4):046801, 2010.

[28] Timothy C Droubay, Lingmei Kong, Scott A Chambers, and Wayne P Hess. Work function reduction by bao: Growth of crystalline barium oxide on ag (001) and ag (111) surfaces. *Surface Science*, 632:201–206, 2015.

[29] Tianyu Ma, Ryan Jacobs, John Booske, and Dane Morgan. Discovery and engineering of low work function perovskite materials. *Journal of Materials Chemistry C*, 9(37):12778–12790, 2021.

[30] Ryan Jacobs, John Booske, and Dane Morgan. Understanding and controlling the work function of perovskite oxides using density functional theory. *Advanced Functional Materials*, 26(30):5471–5482, 2016.

[31] Kenneth J Pérez Quintero, Sergey Antipov, Anirudha V Sumant, Chunguang Jing, and Sergey V Baryshev. High quantum efficiency ultra-

nanocrystalline diamond photocathode for photoinjector applications. *Applied Physics Letters*, 105(12):123103, 2014.

[32] L Velardi, A Valentini, and G Cicala. Highly efficient and stable ultraviolet photocathode based on nanodiamond particles. *Applied Physics Letters*, 108(8):083503, 2016.

[33] AH Sommer and WE Spicer. Bismuth-silver-oxygen-cesium photocathode. *Journal of Applied Physics*, 32(6):1036–1042, 1961.

[34] Alfred H Sommer. Multi-alkali photo cathodes. *IRE Transactions on Nuclear Science*, 3(4):8–12, 1956.

[35] Gaoxue Wang, Ping Yang, Nathan A Moody, and Enrique R Batista. Overcoming the quantum efficiency-lifetime tradeoff of photocathodes by coating with atomically thin two-dimensional nanomaterials. *npj 2D Materials and Applications*, 2(1):1–9, 2018.

[36] Gaoxue Wang, Ping Yang, and Enrique R Batista. Computational screening of two-dimensional coatings for semiconducting photocathodes. *Physical Review Materials*, 4(2):024001, 2020.

[37] EC Aschenauer, S Fazio, JH Lee, H Mäntysaari, BS Page, B Schenke, T Ullrich, R Venugopalan, and P Zurita. The electron–ion collider: assessing the energy dependence of key measurements. *Reports on Progress in Physics*, 82(2):024301, 2019.

[38] A Accardi, JL Albacete, M Anselmino, N Armesto, EC Aschenauer, A Bacchetta, D Boer, WK Brooks, T Burton, N-B Chang, et al. Electron-ion collider: The next qcd frontier. *The European Physical Journal A*, 52(9):1–100, 2016.

[39] Committee on U.S.-Based Electron-Ion Collider Science Assessment, Board on Physics and Astronomy, Division on Engineering and Physical Sciences, and National Academies of Sciences, Engineering, and Medicine. *An Assessment of U.S.-Based Electron-Ion Collider Science*. National Academies Press, Washington, D.C., September 2018.

[40] Reaching for the Horizon: The 2015 Long Range Plan for Nuclear Science, 2015. `http://inspirehep.net/record/1398831/files/2015_LRPNS_091815.pdf` (last Accessed February 1, 2020).

[41] Alpha T N'diaye and Adrian Quesada. Spin-polarized low-energy electron microscopy (spleem). *Characterization of Materials*, pages 1–14, 2002.

[42] Makoto Kuwahara, Soichiro Kusunoki, Yoshito Nambo, Koh Saitoh, Xiuguang Jin, Toru Ujihara, Hidefumi Asano, Yoshikazu Takeda, and Nobuo Tanaka. Coherence of a spin-polarized electron beam emitted from a semiconductor photocathode in a transmission electron microscope. *Applied Physics Letters*, 105(19):193101, 2014.

[43] J. J. Scheer and J. van Laar. GaAs-Cs: A new type of photoemitter. *Solid State Communications*, 3(8):189–193, 1965.

[44] Daniel Pierce and Felix Meier. Photoemission of spin-polarized electrons from GaAs. *Physical Review B*, 13(12), 1976.

[45] Tetsuya Matsuyama, Hiromichi Horinaka, Kenji Wada, Takashi Kondo, Masanori Hangyo, Tsutomu Nakanishi, Shoji Okumi, and Kazuaki Togawa. Spin-dependent luminescence of highly polarized electrons generated by two-photon absorption in semiconductors. *Japanese Journal of Applied Physics*, 40(6A):L555, 2001.

[46] RDR Bhat, P Nemec, Y Kerachian, HM van Driel, JE Sipe, and Arthur L Smirl. Two-photon spin injection in semiconductors. *Physical Review B*, 71(3):035209, 2005.

[47] J.L. McCarter, A. Afanasev, T.J. Gay, J. Hansknecht, A. Kechiantz, and M. Poelker. Measurement of electron beam polarization from unstrained GaAs via two-photon photoemission. *Nuclear Instruments and Methods in Physics Research Section A: Accelerators, Spectrometers, Detectors and Associated Equipment*, 738:149–153, February 2014.

[48] N. B. Clayburn, J. L. McCarter, J. M. Dreiling, M. Poelker, D. M. Ryan, and T. J. Gay. Search for spin-polarized photoemission from GaAs using light with orbital angular momentum. *Physical Review B - Condensed Matter and Materials Physics*, 87(3):1–8, 2013.

[49] Maria Solyanik-Gorgone and Andrei Afanasev. Spin polarization of photoelectrons in gaas excited by twisted photons. *Physical Review B*, 99(3):035204, 2019.

[50] T. Maruyama, E. L. Garwin, R. Prepost, and G. H. Zapalac. Electron-spin polarization in photoemission from strained GaAs grown on GaAs 1 - x P x. *Physical Review B*, 46(7):4261–4264, August 1992.

[51] Xincun Peng, Zhidong Wang, Yun Liu, Dennis M Manos, Matt Poelker, Marcy Stutzman, Bin Tang, Shukui Zhang, and Jijun Zou. Optical-resonance-enhanced photoemission from nanostructured ga as photocathodes. *Physical Review Applied*, 12(6):064002, 2019.

[52] Wei Liu, Yiqiao Chen, Wentao Lu, Aaron Moy, Matthew Poelker, Marcy Stutzman, and Shukui Zhang. Record-level quantum efficiency from a high polarization strained GaAs/GaAsP superlattice photocathode with distributed Bragg reflector. *Applied Physics Letters*, 109(25):252104, December 2016.

[53] Pil Hun Song and K. W. Kim. Spin relaxation of conduction electrons in bulk III-V semiconductors. *Physical Review B*, 66(3):035207, July 2002.

[54] D. T. Pierce, R. J. Celotta, G.-C. Wang, W. N. Unertl, A. Galejs, C. E. Kuyatt, and S. R. Mielczarek. The GaAs spin polarized electron source. *Review of Scientific Instruments*, 51(4):478–499, April 1980.

[55] Jai Kwan Bae, Luca Cultrera, Philip DiGiacomo, and Ivan Bazarov. Rugged spin-polarized electron sources based on negative electron affinity GaAs photocathode with robust Cs $_2$ Te coating. *Applied Physics Letters*, 112(15):154101, April 2018.

[56] N Chanlek, J D Herbert, R M Jones, L B Jones, K J Middleman, and B L Militsyn. The degradation of quantum efficiency in negative electron affinity GaAs photocathodes under gas exposure. *Journal of Physics D: Applied Physics*, 47(5):055110, February 2014.

[57] M. Kuriki, C. Shonaka, H. Iijima, D. Kubo, H. Okamoto, H. Higaki, K. Ito, M. Yamamoto, T. Konomi, S. Okumi, M. Kuwahara, and T. Nakanishi. Dark-lifetime degradation of GaAs photo-cathode at higher temperature. *Nuclear Instruments and Methods in Physics Research Section A: Accelerators, Spectrometers, Detectors and Associated Equipment*, 637(1):S87–S90, May 2011.

[58] H. Sonnenberg. Low-work-function surfaces for negative-electron-affinity photoemitters. *Applied Physics Letters*, 14(9):289–291, 1969.

[59] H. Sonnenberg. Related content On Photoemission from GaAs – Cs – Sb. *Japan. J. Appl. Phys.*, 8:806, 1969.

[60] Tailiang Guo. Novel GaAs photocathodes with alkali antimonide inter-

mediate layers and caesium-oxygen adlayers. *Thin Solid Films*, 281-282(1-2):379–382, 1996.

[61] Minoru Hagino and Ryozo Nishida. Related content Photoemission from GaAs-Cs-Sb (Te). *Jpn. J. Appl. Phys*, 8:123, 1969.

[62] Libin Zhao, Qing Zhou, Shouzhen Zhao, and Baoseng Xie. Study of GaAs-Cs-Sb photoemitter. *Proc. SPIE*, 1982(April 1993):140–144, 1993.

[63] P Michelato, L Monaco, C Pagani, D Sertore, and F Stephan. Cs2Te PHOTOCATHODES ROBUSTNESS STUDIES. *Proceedings of EPAC08*, 2008.

[64] H Sugiyama, K Ogawa, J Azuma, K Takahashi, M Kamada, T Nishitani, M Tabuchi, T Motoki, K Takashima, A Era, and Y Takeda. A study of an electron affinity of cesium telluride thin film. *Journal of Physics: Conference Series*, 298:012014, May 2011.

[65] K Uchida, M Kuriki, Y Seimiya, R Kaku, K Miyoshi, and N Yamamoto. A STUDY ON ROBUSTNESS OF NEA-GAAS PHOTOCATHODE*. *Proceedings of IPAC2014*, 2014.

[66] Jai Kwan Bae, Alice Galdi, Luca Cultrera, Frank Ikponmwen, Jared Maxson, and Ivan Bazarov. Improved lifetime of a high spin polarization superlattice photocathode. *Journal of Applied Physics*, 127(12):124901, March 2020.

[67] J. Kessler. *Polarized Electrons*. Springer, 1976.

[68] C. Jozwiak. *a New Spin on Photoemission Spectroscopy*. PhD thesis, 2010.

[69] J. L. McCarter, M. L. Stutzman, K. W. Trantham, T. G. Anderson, A. M. Cook, and T. J. Gay. A low-voltage retarding-field Mott polarimeter for photocathode characterization. *Nuclear Instruments and Methods in Physics Research, Section A: Accelerators, Spectrometers, Detectors and Associated Equipment*, 618(1-3):30–36, 2010.

[70] Jai Kwan Bae, Matthew Andorf, Adam Bartnik, Alice Galdi, Luca Cultrera, Jared Maxson, and Ivan Bazarov. Operation of Cs-Sb-O activated GaAs in a high voltage dc electron gun at high average current. 2022. To be published.

[71] Report of the Community Review of EIC Accelerator R&D for the Office

of Nuclear Physics, 2017. https://www.osti.gov/servlets/purl/1367855 (last accessed March 26, 2022).

[72] Major Nuclear Physics Facilities for the Next Decade: Report of the NSAC Subcommittee on Scientific Facilities, 2013.

[73] Franco Ciccacci and Gualtiero Chiaia. Comparative study of the preparation of negative electron affinity GaAs photocathodes with O_2 and with NF_3. *Journal of Vacuum Science & Technology A: Vacuum, Surfaces, and Films*, 9(6):2991–2995, November 1991.

[74] Luca Cultrera, Jared Maxson, Ivan Bazarov, Sergey Belomestnykh, John Dobbins, Bruce Dunham, Siddharth Karkare, Roger Kaplan, Vaclav Kostroun, Yulin Li, Xianghong Liu, Florian Löhl, Karl Smolenski, Zhi Zhao, David Rice, Peter Quigley, Maury Tigner, Vadim Veshcherevich, Kenneth Finkelstein, Darren Dale, and Benjamin Pichler. Photocathode behavior during high current running in the Cornell energy recovery linac photoinjector. *Physical Review Special Topics - Accelerators and Beams*, 14(12):120101, December 2011.

[75] R. R. Mammei, R. Suleiman, J. Feingold, P. A. Adderley, J. Clark, S. Covert, J. Grames, J. Hansknecht, D. Machie, M. Poelker, T. Rao, J. Smedley, J. Walsh, J. L. McCarter, and M. Ruiz-Osés. Charge lifetime measurements at high average current using a K 2 CsSb photocathode inside a dc high voltage photogun. *Physical Review Special Topics - Accelerators and Beams*, 16(3):033401, March 2013.

[76] Y. Sun, R. E. Kirby, T. Maruyama, G. A. Mulhollan, J. C. Bierman, and P. Pianetta. The surface activation layer of GaAs negative electron affinity photocathode activated by Cs, Li, and NF3. *Applied Physics Letters*, 95(17):174109, October 2009.

[77] G. A. Mulhollan and J. C. Bierman. Enhanced chemical immunity for negative electron affinity GaAs photoemitters. *Journal of Vacuum Science & Technology A: Vacuum, Surfaces, and Films*, 26(5):1195–1197, September 2008.

[78] C. K. Sinclair, P. A. Adderley, B. M. Dunham, J. C. Hansknecht, P. Hartmann, M. Poelker, J. S. Price, P. M. Rutt, W. J. Schneider, and M. Steigerwald. Development of a high average current polarized electron source with long cathode operational lifetime. *Physical Review Special Topics - Accelerators and Beams*, 10(2):023501, February 2007.

[79] R Alley, H Aoyagi, J Clendenin, J Frisch, C Garden, E Hoyt, R Kirby, L Klaisner, A Kulikov, R Miller, G Mulhollan, C Prescott, P Sáez, D Schultz, H Tang, J Turner, K Witte, M Woods, A.D Yeremian, and M Zolotorev. The Stanford linear accelerator polarized electron source. *Nuclear Instruments and Methods in Physics Research Section A: Accelerators, Spectrometers, Detectors and Associated Equipment*, 365(1):1–27, November 1995.

[80] G. A. Mulhollan. Low-energy polarized electron source test facilities, 1994. SLAC Report No. SLAC-REPRINT-1994-081.

[81] Guy Fishman and Georges Lampel. Spin relaxation of photoelectrons in p -type gallium arsenide. *Physical Review B*, 16(2):820–831, July 1977.

[82] Igor Zutic, Jaroslav Fabian, and S. Das Sarma. Spintronics: Fundamentals and applications. *Rev. Mod. Phys.*, 76(2):323, 2004.

[83] Joseph Z. Terdik, Károly Németh, Katherine C. Harkay, Jeffrey H. Terry, Linda Spentzouris, Daniel Velázquez, Richard Rosenberg, and George Srajer. Anomalous work function anisotropy in ternary acetylides. *Physical Review B*, 86(3):035142, July 2012.

[84] Gabriele Ferrini, Paolo Michelatob, and Fulvio Parmigiani. A MONTE CARLO SIMULATION OF LOW ENERGY PHOTOELECTRON SCATTERING IN Cs2Te. *Solid State Commun.*, 106(1):21, 1998.

[85] Carlo Jacoboni and P. Lugli. *The Monte Carlo Method for Semiconductor Device Simulation*. Computational Microelectronics. Springer-Verlag, Wien New York, 1989.

[86] Masahiko Suzuki, Michihiro Hashimoto, Tsuneo Yasue, Takanori Koshikawa, Yasuhide Nakagawa, Taro Konomi, Atsushi Mano, Naoto Yamamoto, Makoto Kuwahara, Masahiro Yamamoto, Shoji Okumi, Tsutomu Nakanishi, Xiuguang Jin, Toru Ujihara, Yoshikazu Takeda, Teruo Kohashi, Takashi Ohshima, Takashi Saka, Toshihiro Kato, and Hiromichi Horinaka. Real Time Magnetic Imaging by Spin-Polarized Low Energy Electron Microscopy with Highly Spin-Polarized and High Brightness Electron Gun. *Applied Physics Express*, 3(2):026601, January 2010.

[87] R. Vollmer, M. Etzkorn, P. S.Anil Kumar, H. Ibach, and J. Kirschner. Spin-polarized electron energy loss spectroscopy of high energy, large wave vector spin waves in ultrathin fcc co films on cu(001). *Physical Review Letters*, 91(14):1–4, 2003.

[88] Lawrence S. Cardman. The PEPPo method for polarized positrons and PEPPo II. *AIP Conference Proceedings*, 1970(May), 2018.

[89] C. Y. Su, W. E. Spicer, and I. Lindau. Photoelectron spectroscopic determination of the structure of (Cs,O) activated GaAs (110) surfaces. *Journal of Applied Physics*, 54(3):1413–1422, 1983.

[90] N. Kurichiyanil, J. Enders, Y. Fritzsche, and M. Wagner. A test system for optimizing quantum efficiency and dark lifetime of gaas photocathodes. *Journal of Instrumentation*, 14(08):P08025, 2019.

[91] Omer Rahman, Erdong Wang, Ilan Ben-Zvi, Jyoti Biswas, and John Skaritka. Increasing charge lifetime in dc polarized electron guns by offsetting the anode. *Physical Review Accelerators and Beams*, 22(8):083401, August 2019.

[92] M. Rei Vilar, J. El Beghdadi, F. Debontridder, R. Artzi, R. Naaman, A. M. Ferraria, and A. M Botelho Do Rego. Characterization of wet-etched GaAs (100) surfaces. *Surface and Interface Analysis*, 37(8):673–682, 2005.

[93] Cheng Feng, Yijun Zhang, Jian Liu, Yunsheng Qian, Jingzhi Zhang, Jing Zhao, Feng Shi, and Xiaofeng Bai. Optimized chemical cleaning procedure for enhancing photoemission from GaAs photocathode. *Materials Science in Semiconductor Processing*, 91(June 2018):41–46, 2019.

[94] Luca Cultrera, Mark Brown, Siddharth Karkare, William Schaff, Ivan Bazarov, and Bruce Dunham. Alkali azide based growth of high quantum efficiency photocathodes. *Journal of Vacuum Science and Technology B: Microelectronics and Nanometer Structures*, 32(3), 2014.

[95] Cheng Feng, Yijun Zhang, Yunsheng Qian, Jian Liu, Jingzhi Zhang, Feng Shi, Xiaofeng Bai, and Jijun Zou. Improved quantum efficiency and stability of GaAs photocathode using favorable illumination during activation. *Ultramicroscopy*, 202(April):128–132, 2019.

[96] Minoru Hagino and Tadashi Takahashi. Thickness of Cs-Sb films relative to the original Sb films. *Journal of Applied Physics*, 37(10):3741–3743, 1966.

[97] T. Maruyama, D. A. Luh, A. Brachmann, J. E. Clendenin, E. L. Garwin, S. Harvey, J. Jiang, R. E. Kirby, C. Y. Prescott, R. Prepost, and A. M. Moy. Systematic study of polarized electron emission from strained GaAs/GaAsP superlattice photocathodes. *Applied Physics Letters*, 85(13):2640–2642, 2004.

[98] Leonardo Soriano and Luis Galán. Interaction of Cesium-Potassium Antimonide Photocathode Materials with Oxygen: an X-Ray Photoelectron Spectroscopy Study. *Japanese Journal of Applied Physics*, 32(Part 1, No. 10):4737–4744, oct 1993.

[99] A. Galdi, W.J.I. DeBenedetti, J. Balajka, L. Cultrera, M. A. Hines, S. A. McBride, J. B. Baretz, F. Ikponwmen, I. V. Bazarov, and J. M. Maxson. Towards the optimization of photocathode properties via surface science techniques: A study on cs_3sb thin film growth. *Proceedings of NAPAC'19*, page MOPLH24, 2019.

[100] C. W. Bates, Th. M. van Atekum, G. K. Wertheim, D. N. E. Buchanan, and K. E. Clements. X-ray photoemission studies of superficially oxidized cesium antimonide photoemitters. *Applied Physics Letters*, 38(5):387–389, 1981.

[101] Siddharth Karkare, Dimitre Dimitrov, William Schaff, Luca Cultrera, Adam Bartnik, Xianghong Liu, Eric Sawyer, Teresa Esposito, Ivan Bazarov, Siddharth Karkare, Dimitre Dimitrov, William Schaff, Luca Cultrera, and Adam Bartnik. Monte Carlo charge transport and photoemission from negative electron affinity GaAs photocathodes. *Journal of Applied Physics*, 113(104904):2015–2017, 2013.

[102] Xiuguang Jin, Alexandre A.C. Cotta, Gong Chen, Alpha T. N'Diaye, Andreas K. Schmid, and Naoto Yamamoto. Low energy electron microscopy and Auger electron spectroscopy studies of Cs-O activation layer on p-type GaAs photocathode. *Journal of Applied Physics*, 116(17), 2014.

[103] D. G. Fisher, R. E. Enstrom, J. S. Escher, and B. F. Williams. Photoelectron surface escape probability of (Ga,In)As: CsSingle Bond signO in the 0.9 to [inverted lazy s] 1.6 μm range. *Journal of Applied Physics*, 43(9):3815–3823, 1972.

[104] Anthony Frederic John Levi. *Applied quantum mechanics*. Cambridge University Press, 2006.

[105] Robert Gilmore. *Elementary quantum mechanics in one dimension*. JHU Press, 2004.

[106] J. J. Uebbing and L. W. James. Behavior of cesium oxide as a low work-function coating. *Journal of Applied Physics*, 41(11):4505–4516, 1970.

[107] V. V. Bakin, K. V. Toropetsky, H. E. Scheibler, A. S. Terekhov, L. B. Jones, B. L. Militsyn, and T. C.Q. Noakes. P-GaAs(Cs,O)-photocathodes: Demarcation of domains of validity for practical models of the activation layer. *Applied Physics Letters*, 106(18):1–5, 2015.

[108] C Adolphson. A large hadron electron collider at cern, physics, machine, detector. Technical report, LHeC-Note-2011-003-GEN, 2011.

[109] Wei Liu, Shukui Zhang, Marcy Stutzman, and Matt Poelker. Effects of ion bombardment on bulk GaAs photocathodes with different surface-cleavage planes. *Physical Review Accelerators and Beams*, 19(10):103402, October 2016.

[110] J T Yoskowitz, G A Krafft, G Palacios-Serrano, S Wijethunga, J Grames, J Hansknecht, C Hernandez-Garcia, M Poelker, M Stutzman, and R Suleiman. IMPROVING THE OPERATIONAL LIFETIME OF THE CEBAF PHOTO- GUN BY ANODE BIASING. *Proceedings of the 12th International Particle Accelerator Conference*, IPAC2021, 2021.

[111] Jyoti Biswas, Omer Rahman, and Erdong Wang. Study of Photocathode Surface Damage due to Ion Back-Bombardment in High Current DC Gun. *Proceedings of the North American Particle Accelerator Conference*, NAPAC2019, 2019.

[112] Masao Kuriki and Kazunari Masaki. Negative Electron affinity GaAs Cathode Activation with CsKTe Thin Film. *Journal of Physics: Conference Series*, 1350(1):012047, November 2019.

[113] Jyoti Biswas, Erdong Wang, Mengjia Gaowei, Wei Liu, Omer Rahman, and Jerzy T. Sadowski. High quantum efficiency GaAs photocathodes activated with Cs, O $_2$, and Te. *AIP Advances*, 11(2):025321, February 2021.

[114] Omer Rahman, Jyoti Biswas, Mengjia Gaowei, Wei Liu, and Erdong Wang. New Activation Techniques for Higher Charge Lifetime from GaAs Photocathodes. *Proceedings of the 10th Int. Particle Accelerator Conf.*, IPAC2019, 2019.

[115] Alice Galdi, William J. I. DeBenedetti, Jan Balajka, Luca Cultrera, Ivan V. Bazarov, Jared M. Maxson, and Melissa A. Hines. The effects of oxygen-induced phase segregation on the interfacial electronic structure and quantum efficiency of Cs $_3$ Sb photocathodes. *The Journal of Chemical Physics*, 153(14):144705, October 2020.

[116] Bruce Dunham, John Barley, Adam Bartnik, Ivan Bazarov, Luca Cultrera, John Dobbins, Georg Hoffstaetter, Brent Johnson, Roger Kaplan, Siddharth Karkare, Vaclav Kostroun, Yulin Li, Matthias Liepe, Xianghong Liu, Florian Loehl, Jared Maxson, Peter Quigley, John Reilly, David Rice, Daniel Sabol, Eric Smith, Karl Smolenski, Maury Tigner, Vadim Vesherevich, Dwight Widger, and Zhi Zhao. Record high-average current from a high-brightness photoinjector. *Applied Physics Letters*, 102(3):034105, January 2013.

[117] Leo R Dalesio, AJ Kozubal, and MR Kraimer. Epics architecture. Technical report, Los Alamos National Lab., NM (United States), 1991.

[118] P. Emma, R. Akre, J. Arthur, R. Bionta, C. Bostedt, J. Bozek, A. Brachmann, P. Bucksbaum, R. Coffee, F. J. Decker, Y. Ding, D. Dowell, S. Edstrom, A. Fisher, J. Frisch, S. Gilevich, J. Hastings, G. Hays, Ph Hering, Z. Huang, R. Iverson, H. Loos, M. Messerschmidt, A. Miahnahri, S. Moeller, H. D. Nuhn, G. Pile, D. Ratner, J. Rzepiela, D. Schultz, T. Smith, P. Stefan, H. Tompkins, J. Turner, J. Welch, W. White, J. Wu, G. Yocky, and J. Galayda. First lasing and operation of an ngstrom-wavelength free-electron laser. *Nat. Photonics*, 4(9):641–647, 2010.

[119] B. J. Siwick, J. R. Dwyer, R. E. Jordan, R. J. D. Miller, R. S. Dwyer, R. E. Jordan, and R. J. D. Miller. An Atomic-Level View of Melting Using Femtosecond Electron Diffraction: Supp Info. *Science (80-.).*, 458(7234):56, 2003.

[120] R. K. Li and P. Musumeci. Single-Shot MeV Transmission Electron Microscopy with Picosecond Temporal Resolution. *Phys. Rev. Appl.*, 2(2):1–15, 2014.

[121] M J Rhee. Refined definition of the beam brightness. *Phys. Fluids B Plasma Phys.*, 4(6):1674–1676, 1992.

[122] S.I. Anisimov, B.L. Kapeliovich, and T.L. Perel-man. Electron emission from metal surfaces exposed to ultrashort laser pulses. *J. Exp. Theor. Phys.*, 66:375–377, 1974.

[123] W. S. Fann, R. Storz, H. W.K. Tom, and J. Bokor. Direct measurement of nonequilibrium electron-energy distributions in sub-picosecond laser-heated gold films. *Surf. Sci.*, 283(1-3):221–225, 1993.

[124] H. E. Elsayed-Ali, T. B. Norris, M. A. Pessot, and G. A. Mourou. Time-

resolved observation of electron-phonon relaxation in copper. *Phys. Rev. Lett.*, 58(12):1212–1215, 1987.

[125] P. L.E.M. Pasmans, D. C. Van Vugt, J. P. Van Lieshout, G. J.H. Brussaard, and O. J. Luiten. Extreme regimes of femtosecond photoemission from a copper cathode in a dc electron gun. *Phys. Rev. Accel. Beams*, 19(10):1–12, 2016.

[126] Chenjie An, Rui Zhu, Jun Xu, Yaqi Liu, Xiaopeng Hu, Jiasen Zhang, and Dapeng Yu. Increase of intrinsic emittance induced by multiphoton photoemission from copper cathodes illuminated by femtosecond laser pulses. *AIP Adv.*, 8(5), 2018.

[127] A. Bartoli, G. Ferrini, L. Fini, G. Gabetta, F. Parmigiani, and F. Arecchi. Nonlinear photoemission from W and Cu investigated by total-yield correlation measurements. *Phys. Rev. B - Condens. Matter Mater. Phys.*, 56(3):1107–1110, 1997.

[128] H Petek, H Nagano, and S Ogawa. Applied Physics B Hot-electron dynamics in copper revisited: The d-band effect. *Appl. Phys. B*, 68:369–375, 1999.

[129] J. Cao, Y. Gao, and R. Miller. Femtosecond photoemission study of ultrafast electron dynamics on Cu(100). *Phys. Rev. B - Condens. Matter Mater. Phys.*, 56(3):1099–1102, 1997.

[130] Martin Wolf. Femtosecond dynamics of electronic excitations at metal surfaces. *Surf. Sci.*, 377-379:343–349, 1997.

[131] Bärbel Rethfeld. *Mikroskopische Prozesse bei der Wechselwirkung von Festkörpern mit Laserpulsen im Subpikosekundenbereich*. PhD thesis, Technische Universität Carolo-Wilhelmina Braunschweig, 1999.

[132] B. Y. Mueller and B. Rethfeld. Relaxation dynamics in laser-excited metals under nonequilibrium conditions. *Phys. Rev. B - Condens. Matter Mater. Phys.*, 87(3):1–12, 2013.

[133] B. Rethfeld, A. Kaiser, M. Vicanek, and G. Simon. Ultrafast dynamics of nonequilibrium electrons in metals under femtosecond laser irradiation. *Phys. Rev. B - Condens. Matter Mater. Phys.*, 65(21):2143031–21430311, 2002.

[134] Neil W. Ashcroft and N. David Mermin. *Solid state physics*. Saunders College Publishing, 1978.

[135] Zhibin Lin, Leonid V. Zhigilei, and Vittorio Celli. Electron-phonon coupling and electron heat capacity of metals under conditions of strong electron-phonon nonequilibrium. *Phys. Rev. B - Condens. Matter Mater. Phys.*, 77(7):1–17, 2008.

[136] Nikolai Delone. *Basics of Interaction of Laser Radiation with Matter*. Atlantica Séguier Frontières, 1993.

[137] John F. Seely and Edward G. Harris. Heating of a Plasma by Multiphoton Inverse Bremsstrahlung*. *Phys. Rev. A*, 7(3):1064–1067, 1973.

[138] P. B. Johnson and R. W. Christy. Optical constants of the noble metals. *Phys. Rev. B*, 6(12):4370–4379, 1972.

[139] Ralph H. Fowler. The analysis of photoelectric sensitivity curves for clean metals at various temperatures. *Phys. Rev.*, 38(1):45, 1931.

[140] Lee A. DuBridge. Theory of the energy distribution of photoelectrons. *Phys. Rev.*, 43(9):727–741, 1933.

[141] J. H. Bechtel, W. Lee Smith, and N. Bloembergen. Two-photon photoemission from metals induced by picosecond laser pulses. *Phys. Rev. B*, 15(10):4557–4563, 1977.

[142] Gabriele Ferrini, Francesco Banfi, Claudio Giannetti, and Fulvio Parmigiani. Non-linear electron photoemission from metals with ultrashort pulses. *Nucl. Instruments Methods Phys. Res. Sect. A Accel. Spectrometers, Detect. Assoc. Equip.*, 601(1-2):123–131, 2009.

[143] P. Musumeci, L. Cultrera, M. Ferrario, D. Filippetto, G. Gatti, M. S. Gutierrez, J. T. Moody, N. Moore, J. B. Rosenzweig, C. M. Scoby, G. Travish, and C. Vicario. Multiphoton photoemission from a copper cathode illuminated by ultrashort laser pulses in an rf photoinjector. *Phys. Rev. Lett.*, 104(8):1–4, 2010.

[144] Erdong Wang, Joseph Grames, Jiquan Guo, Wei Liu, Vahid Ranjbar, John Skaritka, and Nicholaos Tsoupas. The Design of a High Charge Polarized Preinjector for the Electron-Ion Collider. *Proceedings of the 12th International Particle Accelerator Conference*, IPAC2021:3 pages, 0.689 MB, 2021.